RECONSTRUCTIONS OF LATE PLEISTOCENE MOUNTAIN GLACIER EQUILIBRIUM LINE ALITITUDES AND PALEOCLIMATE IN THE GREAT BASIN

A Thesis
Submitted to the Graduate Faculty
of the
North Dakota State University
of Agriculture and Applied Science

By

Larkin Margaret Walter

In Partial Fulfillment of the Requirements
for the Degree of
MASTER OF SCIENCE

Major Program:
Environmental and Conservation Sciences

April 2022

Fargo, North Dakota

North Dakota State University
Graduate School

Title

RECONSTRUCTIONS OF LATE PLEISTOCENE MOUNTAIN GLACIER EQUILIBRIUM LINE ALTITUDES AND PALEOCLIMATE IN THE GREAT BASIN

By

Larkin Margaret Walter

The Supervisory Committee certifies that this ***disquisition*** complies with North Dakota State University's regulations and meets the accepted standards for the degree of

MASTER OF SCIENCE

SUPERVISORY COMMITTEE:

Benjamin Laabs
Chair

Anne Denton

Stephanie Day

Approved:

April 14th, 2022
Date

Craig Stockwell
Department Chair

ABSTRACT

This thesis presents new reconstructions of paleoglacier surfaces and Equilibrium Line Altitudes in nine mountain ranges in the northeastern Great Basin during the Last Glacial Maximum. Improved methods for paleoglacier and ELA reconstructions were applied in this thesis, using a computationally derived toolset presented by Pellitero et al. (2015, 2016). Additionally, the first computationally derived volume estimates for alpine paleoglaciers in Lake Bonneville are presented. These reconstructions, in addition to ^{10}Be cosmogenic exposure ages taken from the ICE-D website, were used together to further limit the magnitude and climate of the Last Glacial Maximum. Equilibrium Line Altitudes provide a vital link between the mass balance of a glacier and its relationship with climate. Reconstructing these relationships in the Great Basin showed the regional maxima did not coincide with the Lake Bonneville highs stand and the melting of glaciers following the LGM was not the driving factor in the Lake overflow.

ACKNOWLEDGMENTS

I want to sincerely thank my advisor, Ben Laabs, for dedicating hours of his time into my academic development. I feel very fortunate to have worked with someone who is not only an incredibly knowledgeable advisor, but also a good person. I additionally want to thank my committee members, Anne Denton and Stephine Day, who strengthened my research and provided invaluable expertise.

DEDICATION

Doyle Larkin, and Thomas and Anne Walter

It is hard to be unsuccessful in life when you're surrounded by people who never settled for less than their worth. Thanks to the scarifies you made; my life has been privileged beyond measure. You have instilled a kind heart, an open mind and the determination to become whomever I want to be.

TABLE OF CONTENTS

LIST OF TABLES

LIST OF FIGURES

LIST OF ABBREVIATIONS

AABR	Area-Altitude Balance Ratio, the ELA calculation utilized in this thesis. Where the mass-balance gradient of the glacier and the geomorphology is taken into consideration in the calculation.
AAR	Area-Accumulation Ratio considers ELAs to have a 0.50-0.65 accumulation-area to total-area ratio but fails to take hypsometry into consideration.
CIR	Cirque Floor method takes the lowest elevation of the cirque floor to estimate the accumulation zone.
ELA	Equilibrium Line Altitude is a theoretical line on a glacier surface, that's elevation represents where accumulation equals ablation in one year.
LGM	Last Glacial Maximum refers to the last time in Earth history were there was extensive global ice cover. Additionally, this time signifies the culmination of the last Pleistocene glaciation.
LM	Lateral Moraine assumes ELAs are position at the highest lateral moraine elevation.
TCN	Terrestrial Cosmogenic Nuclide exposure dating refers to the use ^{10}Be
THAR	Toe-Headwall Area Ratio calculation assumes ELAs on modern glaciers are located at an elevation that this equates to 35-40% of the total elevation different between the terminus and headwall.

LIST OF SYMBOLS

δ^{18} ..... Delta-O-18 is a measure of the ratio of stable Oxygen 18 and Oxygen 16 isotopes.

^{10}Be..... Cosmogenic nuclides of Beryllium 10 are produced as a result of spallation reaction in quartz bearing glacial erratics.

LIST OF APPENDIX TABLES

1. INTRODUCTION

The termination of the last Pleistocene glaciation occurred ~19 thousand years ago (ka) and cued the start of large-scale global climate changes that spanned until the start of the Holocene ~11.0 ka (Clark et al., 2011). During the last Pleistocene glaciation, western North America featured thousands of discrete alpine glaciers. The geologic remnants of the last glaciation make up much of the mountain valley landscape seen today, including glacial moraines. The widespread distribution of glacial landforms across mountains of the Great Basin reveals a strikingly different glacial climate compared to modern. Alpine glaciers exist as a function of temperature and precipitation, topography, and ice flow (Leonard, 2007) and therefore, provide a measure of climate of the present and, where their former extents can be reconstructed, the past. Geologic records of past glaciers permit reconstructions of past glaciers that can be used to understand paleoclimate change and variability (Ohmura, 1992). Glacial landforms have long been used as the basis for reconstructing the timing and magnitude of glacial advances in the past. When considering the modern warm, arid climate in the Great Basin, the notion of the mountains was occupied by glaciers and valleys by large pluvial lakes only 19 kyr ago can be difficult to conceive. The rapid climatic and hydrologic transition from a region that could house hundreds of alpine glaciers and massive pluvial lakes to the arid desert climate seen today, exemplifies the need for an investigation on climate that surrounded the last Pleistocene glaciation.

Geologic records in the Great Basin were first recognized as exceptional archives of paleoclimate by Gilbert (1890). Glacial chronologies of the Wasatch (Quirk et al. 2020), Uinta, Deep Creek, and South Snake (Laabs and Munroe, 2016), and Ruby and East Humboldt (Laabs et al., 2013) are well developed. Osborn and Bevis (2001) present a thorough synopsis of the

Great Basin glacial morphology and detail past studies done investigating the glacial history of the Great Basin. Before the earliest development of terrestrial cosmogenic nuclide exposure dating (TCN), dating of glacial deposits in the Great Basin relied heavily on radiocarbon dating (Bevis, 1995). Given the Great Basin's excellent inventory of cosmogenic nuclide exposure ages, the timing of the last Pleistocene glaciation throughout the Basin is well understood. Cosmogenic nuclide exposure dating has provided the framework for understanding sub-millennial timescale changes in climate. The timing of glaciation across the Great Basin can be compared to the timing of pluvial lake changes in the Great Basin, such as Lake Bonneville and Lake Lahontan. This relationship represents a unique paleographic setting that allows for the reconstruction of temperature and precipitation. However, the hydrological relationship that existed between mountain glaciers and paleolakes and how it affected the timing of regional glacial maxima is still not well understood. Numerous studies have suggested that Lake Bonneville created a local moisture source in the region that feed alpine glaciers, implying that glaciers and lakes culminated at the same time during the last glaciation (Quirk et al., 2020; Belanger et al., 2020; Laabs and Munroe, 2016). Conversely, Gilbert (1890) and some subsequent researchers suggested that melting of retreating glaciers contributed significantly to the rise of Lake Bonneville and other pluvial lakes in the Great Basin at ~18-16 ka.

The primary factors that contribute to the mass balance of a glacier are temperature and precipitation. Fluctuations to the mass balance of a glacier can be recorded in a shift in ELA, indicating the range of temperature and precipitation need to sustain a glacier. Therefore, the climate that prevails at a glacier ELA is considered sufficient to maintain the existence of glaciers (Ohmura et al., 1992). By taking paleoglacier ELAs during the LGM and comparing them to temperature and precipitations rates that exits for modern ELAs, the magnitude of

climate variation can be inferred. Previous work done by (Lowe, 1971; Leonard 1989; Ohmura et al., 1992) focused on constraining the range of mean summer temperature and mean winter precipitation commonly found at the ELA. Ohmura et al., (1992) quantified an envelope of climate conditions that may have prevailed during the late Pleistocene. Other studies using Ohmura et al. (1992) methods, interested in quantifying the magnitude of change in climate used map based ELAs in the Great Basin (Leonard, 2007; Munroe and Mickelson, 2002; Laabs and Munroe, 2016) and found that the climate conditions that surround the Last Glacial Maximum is thought to have been on the scale of 8-10 °C colder, with similar precipitation to modern.

Pellitero et al. (2015, 2016) present a new set of GIS-enabled tools to facilitate and standardize paleo-glacier reconstructions and subsequent Equilibrium Line Altitudes (ELA). These tools are rooted in the physical relationship of glacier shape, thickness, and flow, and negate the traditional laborious, time-consuming calculations that relied on field data of geomorphic dimensions for reconstructing paleo-glacier shapes and ELAs. Pellitero et al (2015, 2016) tools allow construction of a high-resolution surface of a paleo-glacier, which permit the calculation of true surface area and volume and representation of paleo-glacier surface in a GIS. Subsequently, reconstructed paleo-glacier surfaces can be used to more accurately derive paleo ELAs. Because we do not have geologic proxies for both precipitation and temperature conditions during the last Pleistocene glaciation, paleo-glacier reconstructions are a crucial piece in deriving accurate paleoclimate conditions.

This study presents newly calculated glacier reconstructions, ELAs, volumes, areas, and paleoclimate reconstructions in the Great Basin, United States. The Great Basin encompasses over 40 mountain ranges, of which 9 are examined in this study, all in the northeastern sector of the region: Ruby, Independence, East Humboldt, South Snake, Deep Creek, Oquirrh, Stansbury,

Uinta and Wasatch. The reconstruction of paleoglacier ELAs afford inferences of paleo-temperature and precipitation at the culmination of the last glaciation, which represents the magnitude of subsequent climate change during the transition to the current warm period.

The aim of this thesis is to understand the relationship and timing between mountain glacier maxima and down valley recessional moraines and use their subsequent ELAs to infer paleoclimate that existed. Using the GlaRe tools in GIS, paleoglacier surfaces and paleo ELAs during glacier maxima can be reconstructed. The globally defined climate envelope (Ohmura et al., 1992) can be used in comparison to modern climate found at LGM ELAs, which allows for the estimation of climate that could have existed during the LGM. Constraining the temperature and precipitation that was sufficient to sustain glaciers during the last Pleistocene glaciation provides the key to contextualizing how modern glaciers may respond to similar changing climate conditions.

2. BACKGROUND AND REGIONAL SETTING

2.1. Alpine Glaciers

Glaciers are powerful agents of erosion and deposition, containing complex internal drainage systems that produce large volumes of sediment. For much of Earth history, glaciers have been shaping the landscape, eroding Earth's surface, transporting products of erosion, and depositing these sediments across the land (Bennett and Glasser, 2009). In temperature glaciers, subglacial erosional processes like abrasion and plucking are taking place at the base of the glacier, where the ice at the is at its pressure melting point. These processes deliver entrained sediment to glacier the forefield where it can be deposited at the glacier margin. Over time, the continuous deposition of glacial till along a stable ice margin produces a moraine. Moraines are deposited through ablation of debris-rich ice, glaciotectonic processes such as ice folding and thrusting, debris dumping, or a combination of these processes (Bennett and Glasser, 2009). Moraines afford reconstruction of glacier shape, length, and thickness, and in some instances provide materials suitable for determining their geologic age.

The morpho-stratigraphic position –the relative distance down valley – of moraines in a valley give indications of changes in glacier length through time (Fig. 1). Moraines form at the edge of deposition along a glacier's boundary in the form of either: a lateral, terminal, or recessional moraine. Terminal moraines are positioned furthest down valley during a glaciation and represents the time the glacier was at its greatest length and volume. Recessional moraines are constructed during times when the ice front pauses during overall retreat up valley, indicating either a period of ice-front stability or readvance of the glacier. Recessional moraines can additionally be categorized by their position with relation to the terminal moraine. For example, down valley recessional moraines represent the oldest ice front pause and represents an advance

to almost terminal extents. Glacier's deposit end moraines sequentially, with the terminal moraines being oldest and positioned furthest down valley, and recessional moraines becoming progressively younger up valley. Therefore, moraines record changes in glacier extent from the terminal, maximum phase through recessional phases, giving context to spatial changes in glacier shape and length during previous glaciations and subsequent deglaciation.

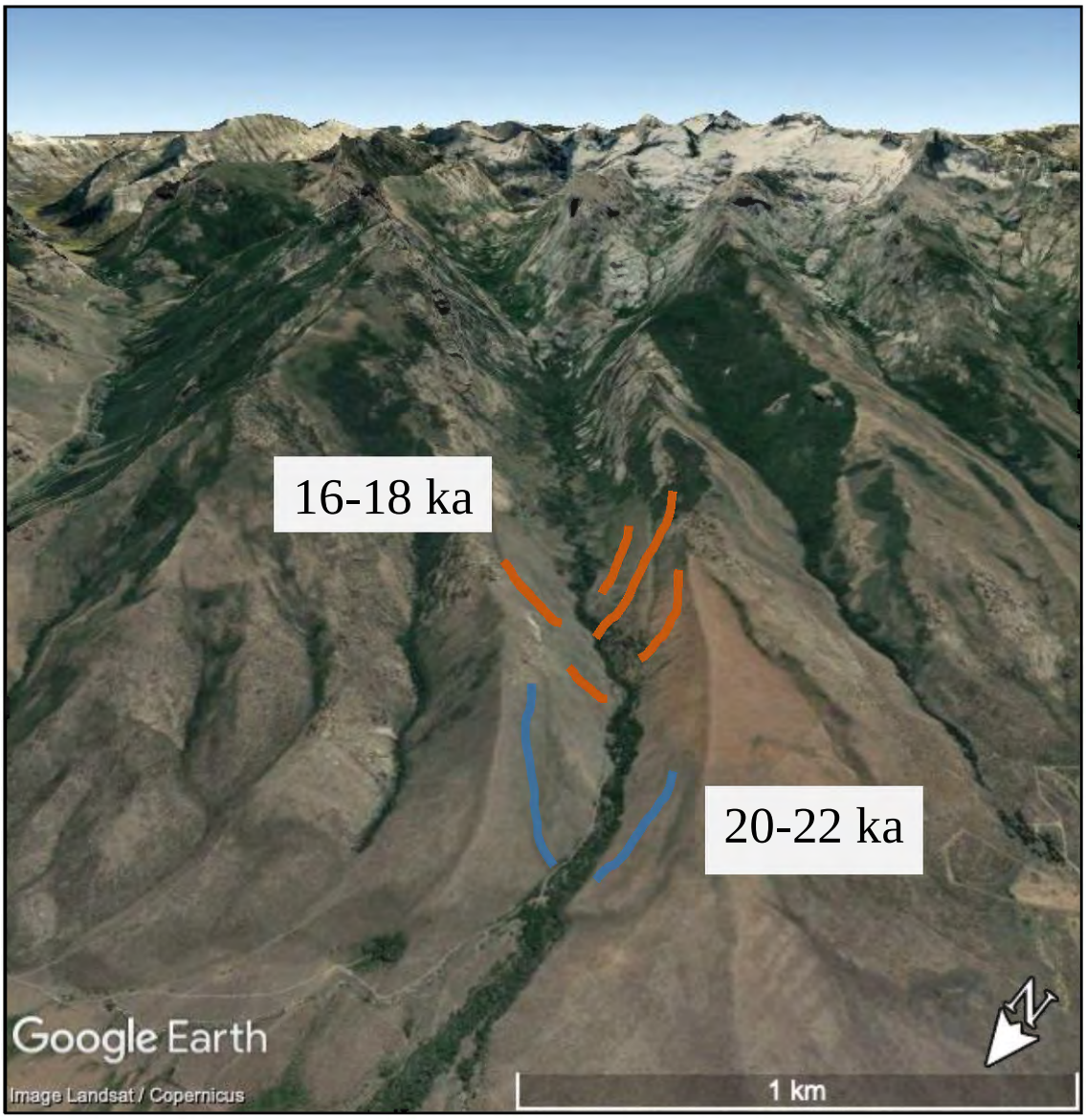

Figure 1. Seitz Canyon, Ruby Mountains, Nevada. Two moraine surfaces are depicted above, the outer moraine outlined in blue represents the terminal moraine deposition in this valley and the inter moraine outlined in orange represents the recessional down valley moraine.

2.2. Pleistocene Glaciations

The Pleistocene Epoch of the Quaternary Period is defined as the time in Earth history that began 2.58 million years ago and lasted until approximately 11,700 years ago (Gradstein et al., 2012). During the Pleistocene, the Earth experienced time intervals of alternating ice expansion and retreat, known as episodes of glaciation and interglaciation. Late Quaternary glacial expansions varied between 80,000 to 120,000 years in duration, each separated by shorter interglacial periods with a recurrence interval of approximately 100,000 years (Denton et al., 2010). The abundance of glacial-interglacial cycles during the last 2.58 million years is unique to the Quaternary Period and is otherwise uncommon over the duration of Earth history. The cyclical nature of the pattern of glaciations has been documented through a variety of paleoclimate records such as moraines, sequences of glacial deposits, and marine sediments recording changes in the global hydrologic cycle (Lisiecki and Raymo, 2005). Among these, marine oxygen isotopes of fossil benthic zooplankton record continuous changes in ice volume, revealing the pace and timing of glaciations and interglaciations (Fig. 2). The time intervals of transition between glacial and interglacial periods on Earth are known as terminations – a period of rapid warming and ice sheet decay lasting only 7-12 kyr. The most recent termination in Earth history occurred after the Last Glacial Maximum, where ice volume on Earth was at its largest extent. The termination lasted from 19.0-11.7 ka, signaling the end of the Pleistocene Epoch and the start of the Holocene Epoch, the current warm period.

Blackwelder (1931) first described evidence of two distinct late Pleistocene glacial advances in the Sierra Nevada that he identified as Tioga (younger) and Tahoe (older). Later, Sharp (1938) identified moraine complexes from two glacial advances in the Ruby and East Humboldt that he classified as Angel Lake (younger) and Lamoille (older). Across the Great

Basin, moraines representing two distinguishable glacier advances and can be identified through their surface morphology, relative location within glacial valleys, and other relative dating techniques (Osborn and Bevis, 2001). The two most recent Pleistocene glaciations in North America are given the term “last,” and the older advance is termed “penultimate.” To identify moraine complexes more precisely, names are given to terminal and recessional moraine complexes based on regionality. The Angel Lake or “last” glacial advance can be easily identified by its well preserved hummocky and bulky topography. Wayne (1984) concluded that the Angel Lake moraines correlate to Late Wisconsinan in age, while the Lamoille deposits correlate to the Illinoian glaciation. Osborn and Bevis (2001), reached the same conclusion, based on relative dating techniques described earlier. Since the Great Basin region is a vast area and includes numerous glaciated mountain ranges, the terms Tioga/Tahoe and Angel Lake/Lamoille are used to define glacial episodes within the same region. The Tioga-Angel Lake and Lamoille-Tahoe episodes are correlative, as verified by TCN exposure dating of moraines and other glacial features from both the Sierra Nevada and interior ranges of the Great Basin (Laabs et al., 2020). Other terms for correlative glacial advances in other regions are the “Pinedale” (last) and “Bull Lake” (penultimate), named for representative moraines in the U.S. Rocky Mountains and “Wisconsin” (last) and “Illinoian” (penultimate), named for deposits of the southern Laurentide Ice Sheet in the Great Lakes lowlands.

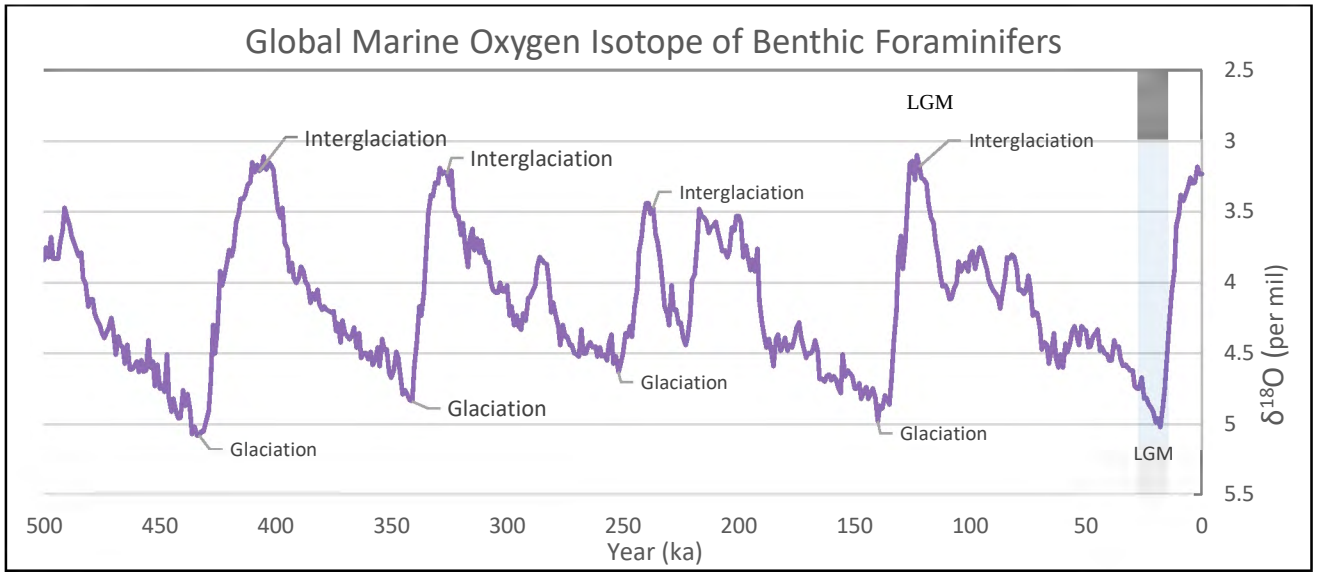

Figure 2. The marine oxygen isotope record of benthic foraminifers compiled by Lisiecki and Raymo (2005). This compilation displays $\delta^{18}O$ records from fifty-seven globally distributed sites that signal shifts from glaciation to interglaciations. The blue bar represents the timing of the LGM (26.5-19.0 ka).

2.3. The Last Glacial Maximum

From 33.0 to 26.5 thousand years ago (ka), ice sheets, globally, grew to their largest extents, where they remained through 26.5-19.0 ka (Clark et al., 2009). This episode of extensive global ice cover signified the culmination of the last glaciation of the Pleistocene Epoch (2.58 million- 11,700 yr). This global climatic episode is known as the Last Glacial Maximum (LGM). During the LGM vast ice sheets expanded, covering much of North America, northern Europe, and Asia (Clark et al., 2009). The timing of the LGM has been constrained by the use of geologic records of paleoclimate, such as studies of marine sediments representing minimum sea level during the LGM (Clark et al., 2009) and marine oxygen isotopes of fossil benthic zooplankton that represent changes in global ice volume through time (Lisiecki and Raymo, 2005). However, because sea level records are an integrated signal of both mountain glacier and ice sheet volume, the timing of regional mountains glacier maxima cannot be resolved from marine oxygen isotopes and sea level records alone. In the western United States, climate conditions that prevailed during the LGM show a great contrast to modern climate. To understand what paleoclimate may have been like during the LGM the timing and magnitude of the last glaciation must be defined.

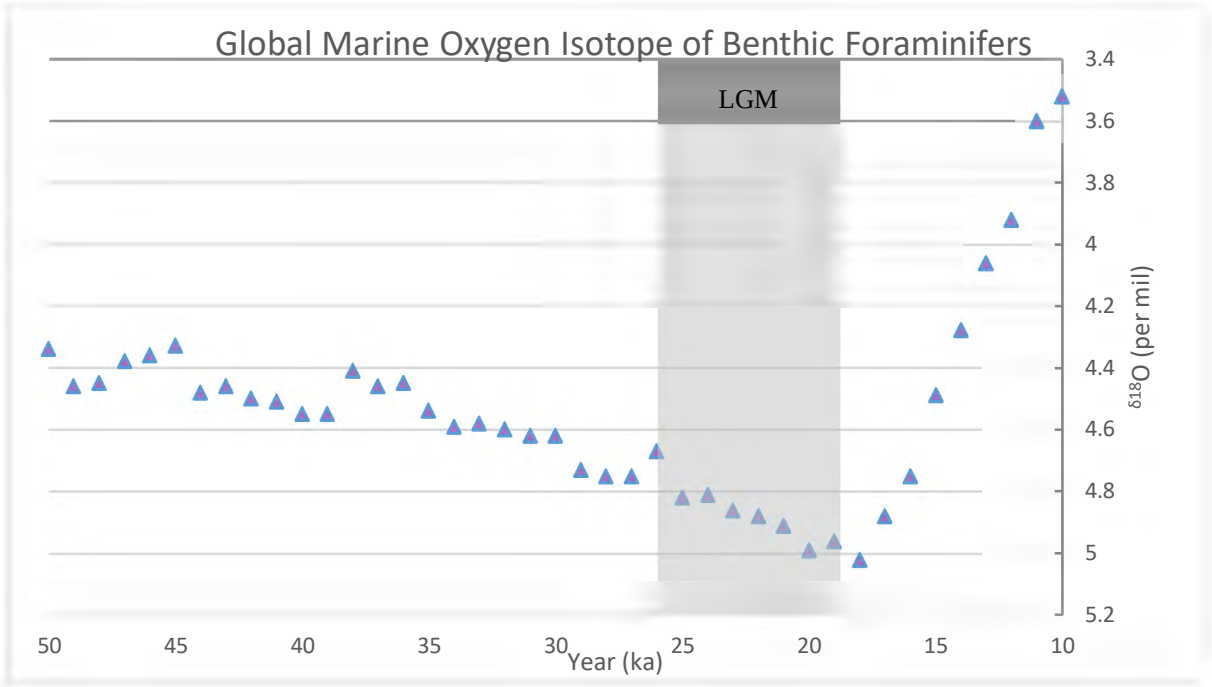

Figure 3. This graph depicts a zoomed in graph of the data from Fig. 2. around the time of the last glacial culmination. The LGM as defined by Clark et al. (2009), can be seen in the gray bar. Following the LGM, $^{\delta 18}O$ concentration around 17.0 ka begin to decrease, indicating a global scale warming.

2.4. Terrestrial Cosmogenic Nuclide Exposure Dating

Over the past three decades, terrestrial cosmogenic nuclide (TCN) exposure dating techniques have transformed our understanding of the temporal distribution of glaciers across the globe (Laabs et al., 2020; Young et al., 2011; Jomelli et al., 2011, 2014; Shakun et al., 2015; Heyman et al., 2019). The expansion of TCN inventory has allowed for more precise numerical age limits on glacial deposits and interpreting the timing of Pleistocene glacial advances across western North America, which could not previously be estimated using traditional dating methods such as carbon-14 dating. TCN exposure dating relies on precise calculations of the production of cosmogenic nuclides in surface material through time and accurate measurement of the concentration of cosmogenic nuclides in surface material. This geochemical change is the result of the interaction between glacially sourced materials and cosmic radiation (Rossi, 1964).

Matter exposed to cosmic radiation undergoes characteristic changes in its chemical composition (Lal and Peters, 1967). These changes in composition are largely a result of a nuclear cascade reaction, called a spallation reaction that results in the production of cosmogenic nuclides. In solid material at the Earth surface, the spallation reaction occurs within a mineral lattice and produces terrestrial cosmogenic nuclides, which can be stable (e.g., neon-21, helium-3) or radioactive (e.g., chlorine-36, aluminum-26, or beryllium-10). The predicted concentration of the terrestrial cosmogenic nuclide depends on numerous factors affecting the production rate at the Earth surface, including composition of the material, its geographic latitude and altitude, the erosion rate, whether the sample is continuously exposed (Borchers et al., 2016). The geographic variation of cosmogenic-nuclide production rates reflects two things, primarily altitude due to the shielding effect of the atmosphere and secondarily the position in the Earth's magnetic field, represented by the geomagnetic longitude. As a result of this shielding effect, production rates are greater at higher elevations (Balco, 2011). For an accurate age to be obtained two requirements need to be met: an accurate measurement of the nuclide concentration, achieved through proper sampling and lab techniques, and an accurate estimate of the nuclide production rate, achieved through scaling models (Balco, 2011). The latter has proven the trickiest part of obtaining ages because of the complexity of the calculation and the lack of accurately measured nuclides of interest. Estimating nuclide production rates rely on two elements that can be summarized by a scaling scheme and a calibration set, derived from nuclide concentrations measure in one or more areas where the exposure age is independently known (Balco, 2011). The middle layer calculations in this analysis utilize version 3 online exposure age calculator, the first version to implement scaling methods presented by Lifton et al. (2014).

Glacial erratics are tall, monumental boulders deposited atop moraines by glacier ice and are commonly targeted for TCN exposure dating of moraines. Erratic's that are ideal targets for TCN exposure dating are quartz bearing rocks that have undergone little or no erosion and have been continuously exposed to cosmic radiation. Quartz is made up almost entirely of silicon and oxygen, making it an ideal target mineral for the production of cosmogenic beryllium-10 (10Be) at the Earth surface. In theory, erratic boulders at a moraine crest would be expected to have similar exposure ages if they were deposited by glacier ice at the same time, however, differences can arise due to variability in surface exposure or erosion at the boulder surface. To reduce error, boulders should meet a set of criteria. Selected boulders (1) have not been significantly covered in snow, (2) no visible erosion has taken place on the boulders surface, (3) the boulder was not previously exposed to cosmic rays before its deposition on the moraine crest. These criteria can be difficult to fully assess, and therefore most applications of TCN exposure dating to moraines involve sampling multiple erratic boulders on a single moraine surface and using either the oldest or average boulder exposure age as the time when the moraine was last occupied by glacier ice.

Through the application of TCN, researchers have been able to better constrain the timing of different Pleistocene glacial episodes and have identified times of moraine deposition during the last Pleistocene glaciation. Many studies using TCN exposure dating have focused on dating terminal moraines, with the intent of constraining the timing of the last glacial maximum within a given mountain range or region (Licciardi et al., 2004; Porter and Swanson, 2008; Laabs et al., 2013; Wesnousky et al., 2016; Benson et al., 2005; Marchetti et al., 2005, 2007; Laabs et al., 2020). This dating method provides the critical temporal information needed to have a

comprehensive understanding of how glaciers advance and retreat through time and affording the use of glacial chronologies as a paleoclimate record for glacier change in time and space.

2.5. Equilibrium Line Altitudes

The Equilibrium Line Altitude (ELA) of a glacier represent a hypothetical line that divides the glacier into an upper zone, that experienced net accumulation of snow and ice, and a lower zone that experienced net ablation of snow and ice, while a glacier occupied a moraine. Accumulation of snow or ice occurs during the coolest months of a water year (for modern glaciers in North America, October-June), and ablation of snow or ice occurs during warmer months (July-September, Fig. 4). Therefore, the ELA resides at the elevation on a glacier where at the end of the ablation season the net mass gained or lost is zero. The existence of land-terminating glaciers is controlled mainly by climate, chiefly temperature and precipitation (Ohmura et al., 1992). However, previous work on ELAs demonstrate that regional ELAs are influenced not only air temperature and summer ablation, but also climatic variables during the ablation season such as shortwave radiation, spatial distribution of cloud cover, warm advection due to wind and the proportion of rain to snow (Meierding, 1982). ELAs can be used to understand climate in two ways, the first is with regards to the impact of accumulation has on the energy-balance of the glacier. This approach focuses on understanding how the addition of new mass transfers to the actual size and physical characteristics of the glacier. And the second approach aims to understand the statistical relationship that exists between temperature and precipitation need to sustain an ELA at a specific elevation (Ohmura et al., 1992).

Each glacier possesses a unique and quantifiable mass-balance sensitivity relationship with regards to the ELA (Ohmura et al., 1992). Glaciers mass balance is mainly controlled by temperature, precipitation, shear stress and flow. The winter mass balance of a glacier has been

directly correlated to meteorological precipitation (Ohmura et al., 1992), justifying the approximation that annual precipitation is a quantifiable through winter balance and summer precipitation. Where climate is sufficient to maintain glaciers, year-to-year variations of the ELA can be a good indicator of the variation of total mass balance of a glacier (Ohmura et al., 1992). An increase in the mass of a glacier will drive the ELA to a lower elevation and conversely, a negative mass balance will drive the ELA to a higher elevation. The climate prevailing at the ELA is categorizes as a function of annual total precipitation and summer temperatures in the free atmosphere (Ohmura et al., 1992). Because the ELA is controlled mainly through winter precipitation, and summer air temperature, variations of ELAs can be directly attributed to changes in local climate conditions. By having an established relationship between precipitation and temperature at the ELA, it makes it possible to determine one of those conditions, provided the other is known. In the interior western United States, glaciers were more sensitive to temperature during the ablation season, which can be inferred from reconstructed ELAs (Meierding, 1982; Munroe and Mickelson, 2002).

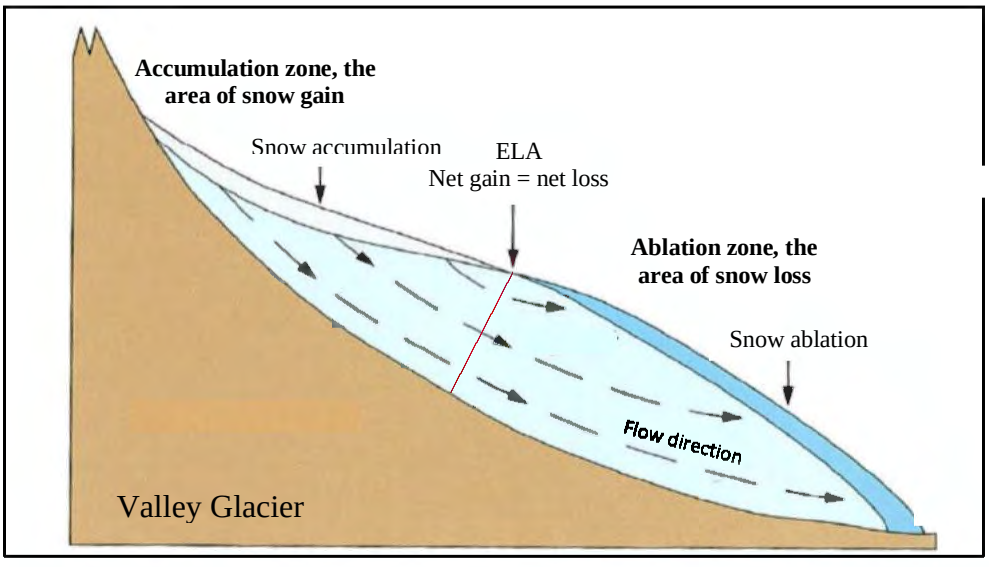

Figure 4. A typical valley glacier has an accumulation zone where snow is gained, and an ablation zone where snow is lost. The two zones are separated by an ELA that quantifies this relationship. (Hambrey and Alean, 2004)

Glacier ELAs have widely been used to infer past and present climate conditions, many studies have been done demonstrating the relationship between regional climate and ELA trends (Meierding, 1982; Ohmura et al., 1992; Munroe and Mickelson, 2002; Leonard, 2007; Laabs et al., 2011). Munroe and Mickelson (2002) calculated ELAs for nineteen northern Uinta glacial valleys based on glacial landforms such as lateral and end moraines to reconstruct paleoglacier shapes. They outline four different methods for calculating ELAs: Area-Accumulation Ratio (AAR), toe-headwall altitude ratio (THAR), highest elevation of lateral moraines (LM), and cirque floor (CIR). Additionally, Pellitero et al. (2015) presents methods for calculating ELAs using the Median Glacier Elevation (MGE) method and Area-Altitude Balance Ratio (AABR). All previous methods listed can be separated into two categories; calculations that rely solely on the position with regards to elevation of glacial landforms, such as moraines, and those that also require the geometry of the paleoglacier surface (Pellitero et al., 2015). Munroe and Mickelson (2002) concluded that the AAR, THAR, and LM methods yielded better surfaces than the CIR because they contained similar standard deviations. Additionally, the means of those three are statistically indistinguishable between the AAR and THAR, AAR and LM, and THAR and LM. Moreover, Pellitero et al., (2015) describes the AAR method as being the most widely used method for calculating paleo ELAs. However, it fails to take the hypsometry of a glacier into consideration, and is therefore, not as robust as the AABR method.

2.6. Lake Bonneville Basin

2.6.1. The Great Basin

The Great Basin region of southwestern North America is an internal drainage system, positioned in the rain shadow of the Sierra Nevada mountains, and encompasses parts of California, Utah, Idaho, Nevada, and Oregon (Fig. 5). By virtue of the Great Basin's position

with regards to the Sierra Nevada rain shadow, climate is dry with hot summers and cold winters and large daily variability (Osborn and Bevis, 2001). The Great Basin's most notable features are both its arid climate, and basin-and-range topography. Osborn and Bevis (2001) describe the geographic extent of the Great Basin as bound in the west by the Sierra Nevada and Cascade Ranges, on the south by the part of the Mojave Desert drained by the Colorado River, on the south and east by the Colorado Plateau, and on the north by the Snake River Plain. Forty glaciated mountain ranges are in the Great Basin and are scattered across 200,000 square miles, with generally north-south-trending, elongated, normal fault bounds (Osborn and Bevis, 2001). Fifteen of those glaciated mountain ranges, were present within the hydrological basin of Lake Bonneville.

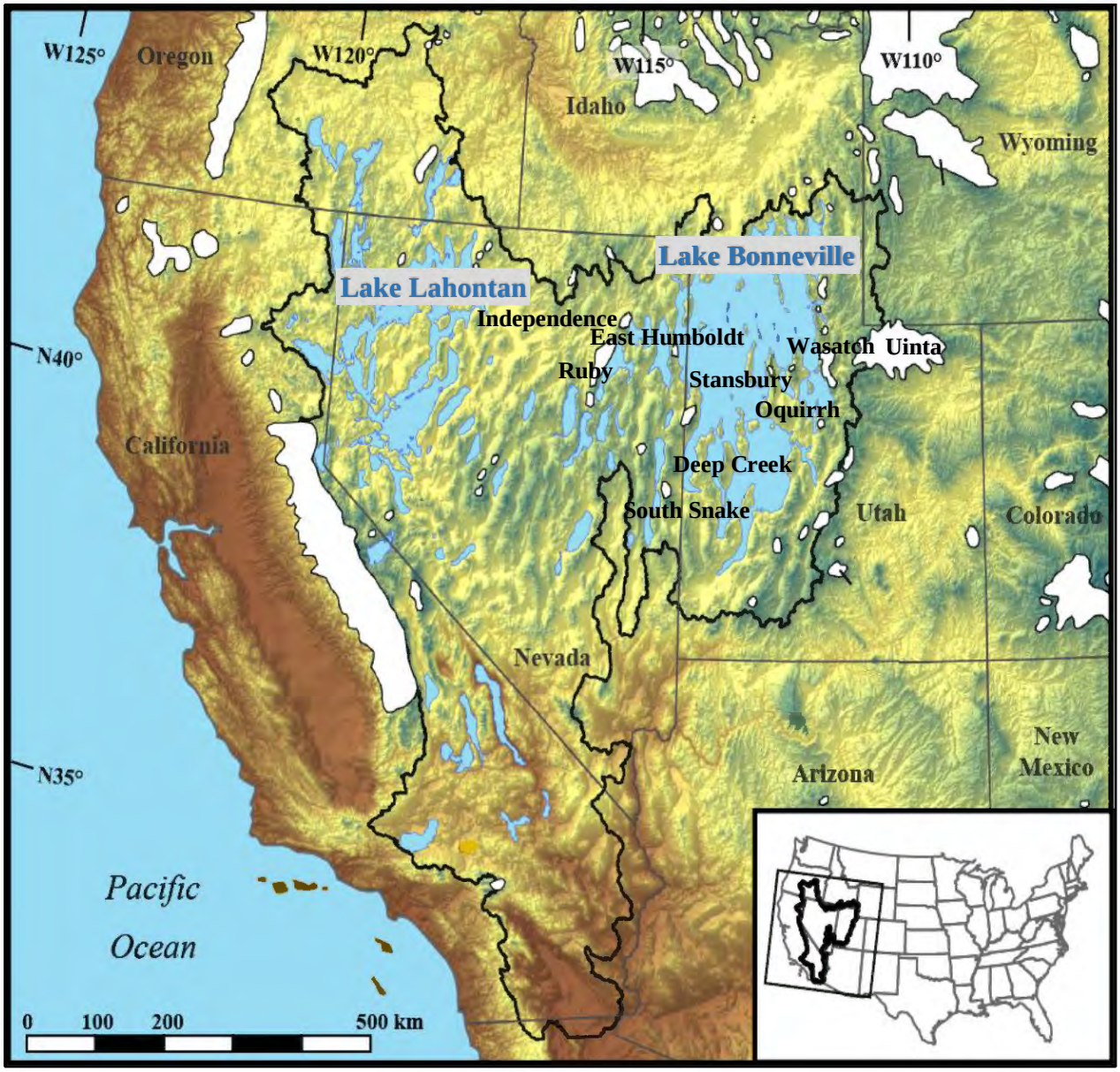

Figure 5. The Great Basin at the LGM. Overview of glacier extents in the Great Basin during the last glacial maximum. The black outline represents the boundary of the Great Basin, where paleo-lakes are shown in light blue and paleo glacier extents are shown in white. Depicted on this map is Lake Bonneville and Lake Lahontan and the nine mountain ranges included in this study: Independence, East Humboldt, Ruby, South Snake, Deep Creek, Stansbury, Oquirrh, Wasatch and Uinta mountains.

Many studies (Hostetler et al., 1994; Carpenter, 1993; Laabs and Munroe 2016; Munroe and Mickelson 2002; Leonard, 2007) have been done examining the increased moisture availability that Lake Bonneville could have provided to mountain glaciers in the Great Basin.

The abundant and clear stratigraphic relationships between glacial and lacustrine deposits in the Great Basin has led to a more precise understanding of the relative timing of glacier maxima and lake high stands. Additionally, the presence of Lake Bonneville, who is at its largest extents covered an area of 51,700 km^2 (O'Connor, 1993), allows for the assessment of regional hydroclimate variations across the Basin. Laabs et al. (2006) and Munroe et al. (2006) examined Pleistocene glaciation in the Great Basin and suggest that Pleistocene glaciers on the downwind side of Lake Bonneville, experienced local precipitation enhancement. Comparatively, Hostetler et al. (1994) indicated that precipitation in the Bonneville basin, specifically near the, was significantly enhanced by the presence of the lake. Lake-effect storms develop over Great Salt Lake today, depositing significant snowfall in the Wasatch and western Uinta Mountains (Carpenter, 1993), and may have been greater in magnitude when the lake was larger (Hostetler et al., 1994). The area of Lake Bonneville accounted for nearly, ¼ of the whole Great Basin and had a clear impacted on the climate of the Basin. An assessment of regional paleoclimate, ELAs and glacier reconstructions in the Great Basin would not be complete without a comprehensive understanding of relationship between alpine glaciers and Lake Bonneville.

2.6.2. Glaciated Mountain Ranges

Positioned on the furthest west side of the Great Basin is the Sierra Nevada, a tall and narrow mountain range that parallels the California/Nevada border. The Sierra Nevada was the largest valley glacier system in the Great Basin, with the eastern valley flanks draining directly into the Great Basin. Well preserved moraine complexes have led to a deep understanding of the glacial chronology in the Sierra Nevada, which contains a plethora of Chrlorine-36 and Beryllium-10 TCN exposure ages.

On the opposite side of Nevada, close to the Nevada/Utah border is a 200-km-long mountain chain, the East Humboldt and Ruby Mountains, which are centrally located within the Great Basin. During the last Pleistocene glaciation, the Ruby and East Humboldt Mountains hosted more than 130 valley glaciers over 150 km, represented by high-relief lateral moraines and lower-relief end moraines (Laabs et al., 2013). Around the timing of the last glaciation these two ranges were located between areas occupied by the two largest Pleistocene lakes in the Great Basin, Bonneville, and Lahontan.

South of the Ruby and East Humboldt Mountains, on the Nevada/ Utah border lies the Deep Creek and South Snake Range the latter being home to Great Basin National Park and the only remaining glacier in the Great Basin (Osborn and Bevis., 2001). The Deep Creek Range and South Snake Range hosted smaller glaciers than the Ruby and East Humboldt Mountains were near the southwestern edge of Lake Bonneville, with glacial valleys draining into Lake Bonneville.

At the border of the Great Basin are the Middle Rocky Mountains, where the Wasatch Range trend north-south and were heavily glaciated during the Pleistocene glaciations (Laabs and Munroe 2016), as indicated by an abundance of glacial-erosional landforms and moraines representing the last two Pleistocene glaciations (Quirk et., 2020). The Wasatch Mountains drained into Lake Bonneville and were directly downwind of the lake. Due to the close proximity and drainage of the Wasatch front into Lake Bonneville, this region's glacial temporal patterns have long been explored. In fact, the dating of moraine deposits through stratigraphy, radiocarbon dating and terrestrial exposure dating in conjunction with the Lake Bonneville high stand has been investigated for over a century, with the first accounting of glacial and lake deposits described by Gilbert (1890).

Directly east of the Wasatch Mountains in northern Utah lie the Uinta Mountains, an east-west-trending range that drains partially into the Colorado River and partially into the Great Basin. During the last glaciation, the western Wasatch and the Uinta Mountains featured the largest valley glacier systems in Utah (Laabs et al., 2011). Among glaciated regions of the western U.S, the Uinta Mountains are widely known for their glacial geomorphology and unique east-west orientation that extends more than 150 km and contain the highest peaks in Utah. Additionally, the range features north-south-trending glacial valleys on the western side; Provo River, Bear River, and Weber River that flow directly into Great Salt Lake and are therefore part of the Bonneville Basin (Laabs and Munroe, 2016). Conversely, the eastern side of the range makes up a collection of the Middle Rocky Mountains that flows into the Colorado River.

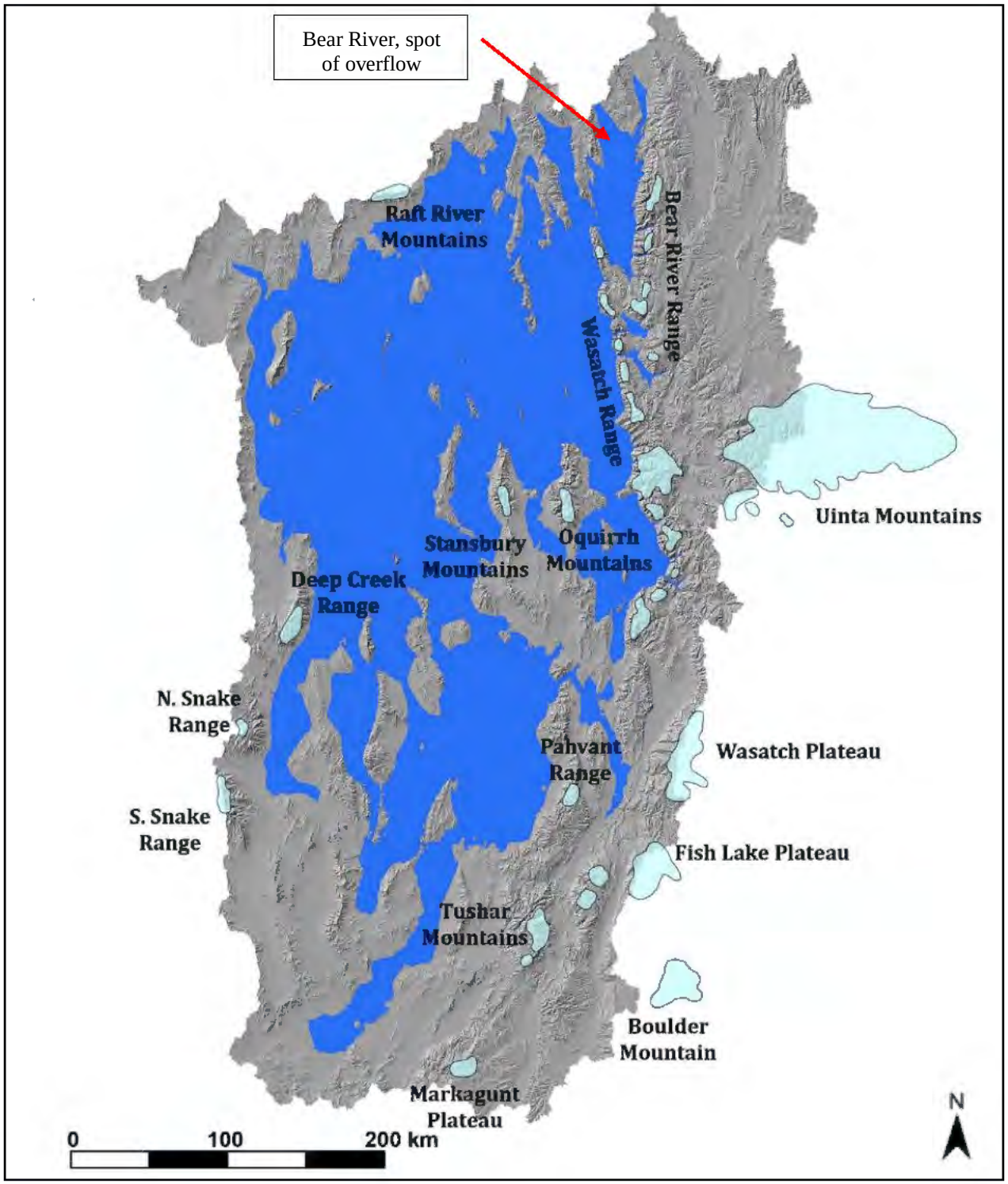

Figure 6. Relief map of Lake Bonneville basin, with the maximum extent of Lake Bonneville shown in blue and Pleistocene valley glaciers are in transparent light blue, with black boxes around the mountain ranges of interest. Mapping of paleoglacier redrawn by Laabs and Munroe (2016), originally drawn by Bob Beik in 2010.

2.6.3. Lake Bonneville

Located within the Great Basin was the Bonneville Basin, named after the largest Pleistocene paleolake in the region, Lake Bonneville. Lake Bonneville was primarily fed by the Bear, Weber, and Provo rivers, which drained from the Wasatch and Uinta Mountains (Belanger et al., 2021). Oviatt (2015) records Lake Bonneville's maximum surface area as 50,000 km^2. The majority of ice volume was concentrated to the east side of Lake Bonneville in the Wasatch and Uinta Mountains, although the total volume of mountain ice was likely less than 5% of the volume of Lake Bonneville (Laabs and Munroe, 2016). Increased effective moisture throughout the late Pleistocene, driven by decreased regional temperature and/or increased regional precipitation, supported the formation of pluvial lakes across the Great Basin.

During the last Pleistocene glaciation, the hydrological basin of Lake Bonneville housed fifteen different glaciated mountain ranges. As the largest of the Great Basin pluvial lakes, Lake Bonneville's rise and fall is a critical recorder of regional hydrologic change in the Great Basin (Belanger et al., 2021). The history of the Bonneville Basin can be subdivided into three phases, the transgressive phase (30-18 ka), the overflowing phase (18-15 ka), and the regression phase (15-12.5 ka) (Laabs and Munroe, 2016) (Fig. 7). During the latter part of the LGM, Lake Bonneville, along with most pluvial lakes in the Great Basin reached their maximum extents from 21.0 to 15.0 ka (Belanger et al, 2021). During the transgressive phase, the lake occupied a hydrographically closed basin, this resulted in the lake being sensitive to changes in climate and experiencing a series of oscillations and fluctuations in response to changes in its water budget (Oviatt, 2015). Lake Bonneville began expanding prior to the Last Glacial Maximum (LGM; 26.6–19.0 ka; Clark et al., 2009) and reached its highest shoreline by 18.0 ka. The pattern of

mountain glaciation in the northeastern Great Basin suggests that paleolakes affected the mass balance of mountain glaciers in the region (Laabs et al., 2011).

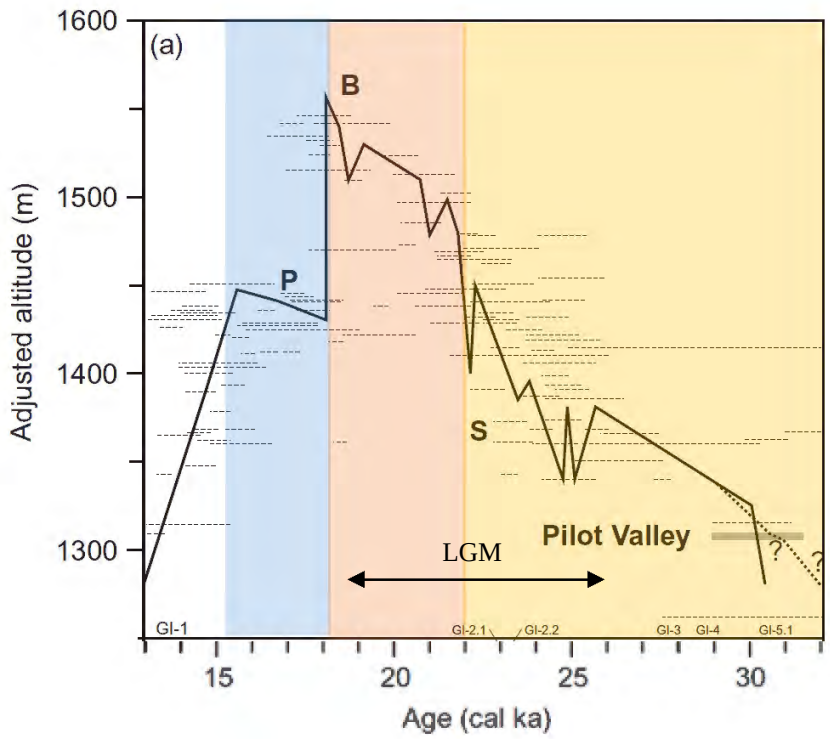

Figure 7. Lake Bonneville hydrography with calibrated radiocarbon ages shown as thin dashed lines, illustrating the timing and elevations of major shorelines. Major shorelines: P, Provo or overflowing shown in blue, B, Bonneville shown in orange, S, Stansbury shoreline shown in yellow (From Miller and Phelps, 2016).

Laabs et al. (2006) and Munroe et al. (2006) suggest that glaciers in the Uinta Mountains, as well as those in the Wasatch Range, experienced local precipitation enhancement which appears to be supported by this study. Regional climate modeling (Hostetler et al., 1994) also indicates that precipitation in the Bonneville basin, particularly near the lake, was significantly enhanced by the presence of the lake. Lake-effect storms develop over Great Salt Lake today, depositing significant snowfall in the Wasatch and western Uinta Mountains (Carpenter, 1993), and may have been greater in magnitude when the lake was larger (Hostetler et al.,

1994). Because of this enhanced precipitation may have additionally been seen in the Stansbury, Oquirrh, Wasatch, and western Uinta Mountains and augmenting glacier mass balance.

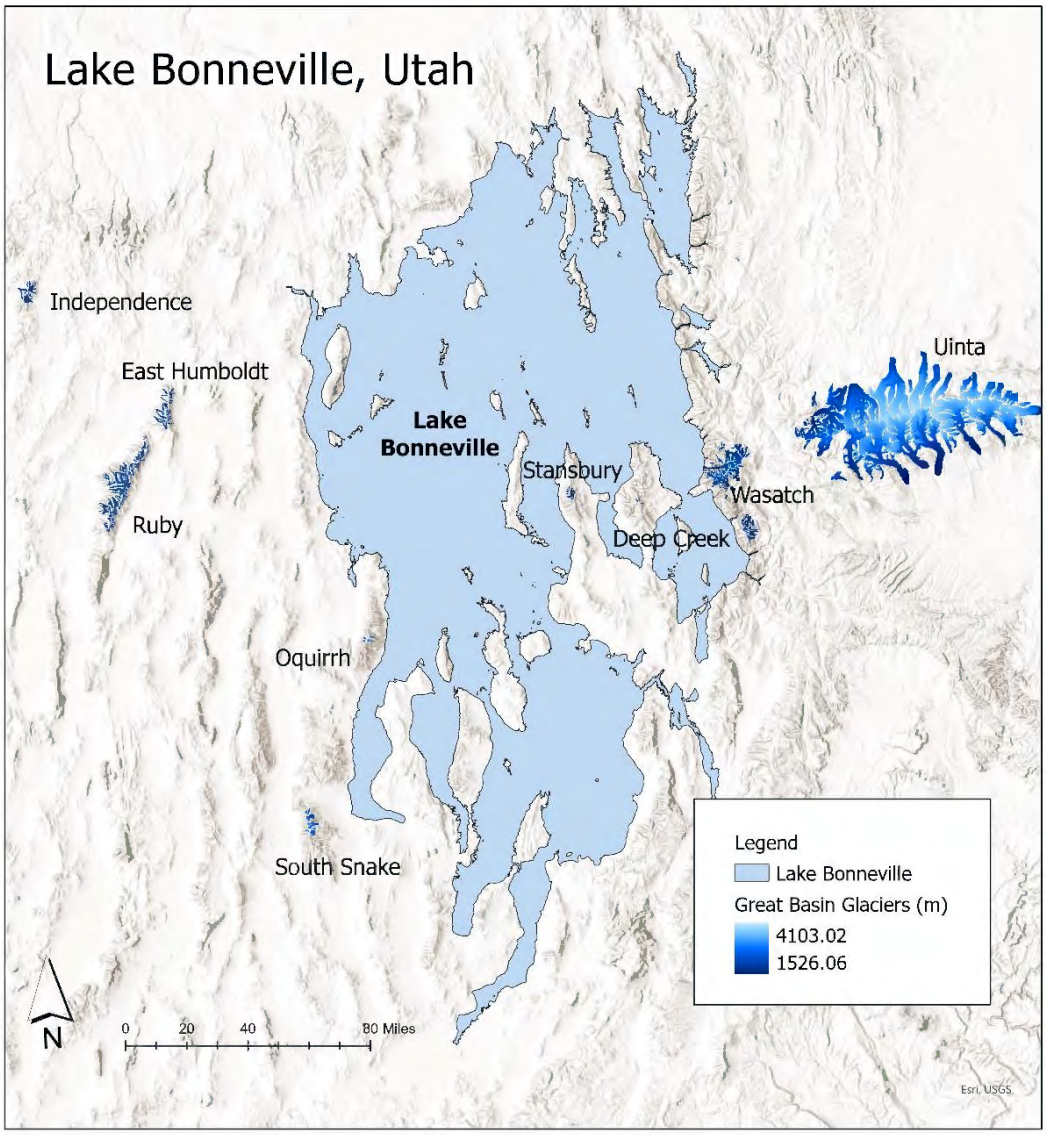

Figure 8. The layout of the Great Basin during the LGM ~ 20,000 ka. Ranges are listed from west to east: Independence, Easy Humboldt, and Ruby Mountains of Nevada and the Oquirrh, South Snake, Stansbury, Deep Creek, Wasatch, and Uinta Mountains of Utah. Positioned in central-northern Utah was the paleo-lake Bonneville, the Great Salt Lake stands as the ruminants of Lake Bonneville today.

2.7. Late Pleistocene Climate in the Bonneville Basin

Over the last 20,000 years, the Great Basin has undergone a major hydroclimatic shift from a cool, wet region with a climate that could house abundant lakes and mountain glaciers, to

a desert in which surface water is relatively sparse. During the LGM, Oster et al. (2015) identified evidence of a precipitation dipole interaction in western North America, in the southwestern region there was comparatively wetter conditions and drier conditions in the northwest, closer to the Laurentide and Cordilleran Ice Sheets. A recent study by Tierney et al. (2020) reconstructed surface air temperature during the LGM based on a large compilation of paleoclimate data. They found evidence of large-scale cooling across the North Hemisphere, with the strongest cooling near 40°, the latitude that coincides with the northern the Great Basin. A hydrological model of temperature and precipitation in the Great Basin (Belanger et al., 2021) suggests that the region was cold and dry during the LGM, after which precipitation increased gradually until roughly 15.0 ka. Specifically, during the LGM interval (~21–20 ka) Lake Bonneville was able to approach its highest water level under conditions roughly 9.5°C colder but only 7% wetter than today. During the latter part of the LGM, Lake Bonneville, along with most other pluvial lakes in the Great Basin, expanded in area and volume to form a large, overflowing lake from 18.0- 15.0 ka (Belanger et al., 2021). This implies that it was not just an increase in precipitation that caused glaciers to advance and lakes to rise, but a depression of temperature coupled with wetter conditions. However, the magnitude of air temperature and precipitation change that would have favored the expansion of glaciers during the LGM has not yet been established.

The well-established stratigraphy of Lake Bonneville's shoreline progression provides a key chronological record of the hydrologic cycle in the Great Basin during the Late Pleistocene. However, the relationship between valley glaciers in the Great Basin and how their mass contributed to the overflow of Lake Bonneville and vis versa is still relatively unknown. By doing region-wide paleo glacier reconstructions and identifying discrepancies in ELA elevation

estimates, we can provide a valuable indication of both the intensity and nature of climatic change that occurred as a result of the LGM.

3. COSMOGENIC CHRONOLOGY OF THE LAST GLACIATION IN THE BONNEVILLE BASIN

3.1. Terrestrial Cosmogenic Nuclide Exposure Dating

The glacial geology of the Great Basin has been of scientific interest for almost a century. Hauge and Emmons (1877) conducted the first U.S Geological exploration in 1877, and later the first reports of glacial deposits were written by Blackwelder (1931, 1934). By reading the geomorphological characteristics Blackwelder (1931) was the first to identify evidence of two distinct glaciations in the Great Basin. With the invention of TCN exposure dating the timing of these two glacial advances could be understood in the context of the Great Basin. Much like radiocarbon dating, TCN dating utilizes the preservation of materials to measure rates of geologic process that can determine the timing of glacier and ice sheet advance and retreats. Most studies involving TCN dating focus on the last glaciation with less emphasis on the penultimate glaciation (Laabs et al., 2013). The Angel Lake moraines which correlate to the last Pleistocene glaciation constructed from cirque, valley and piedmont glaciers typically contain frequent boulders and a degree of weathering. The surfaces of the moraines tend to be steep-fronted, broad hummocky and contain relatively sharp crests (Osborn and Bevis, 2001). All moraine crests feature large erratic boulders with a variety of quartz-rich lithologies (Laabs et al., 2013), including: migmatite, pegmatitic granite, gneiss, monzonite, and quartzite.

3.2. ICE-D

As TCN exposure dating has become the primary dating method for Pleistocene Mountain glacial deposits and landforms and with nearly 10,000 cosmogenic nuclide measurements published in the literature, there was motivation to create a computational and data management infrastructure to represent geochemical data needed to compute cosmogenic

exposure ages. The Informal Cosmogenic Exposure Age Database (ICE-D; http://ice-d.org; Balco, 2020) provides such infrastructure, providing a compilation of cosmogenic nuclide geochemical data and TCN exposure ages of glacially sourced materials, spanning all seven continents (Fig. 9). In contrast to other services that aim to archive geochronological data, the ICE-D database is not structured as single entity but instead is an application that functions to serve collections of data need for specific analyses (Balco, 2020). ICE-D is, therefore, subdivided into three databases, (1) Antarctica, (2) Greenland and (3) Alpine, the latter is used to synthesize glacial chronologies for this thesis.

A unique component of ICE-D is a transparent middle layer that serves derived geologic information about cosmogenic nuclide production rates and computes TCN exposure ages or erosion rates. The calculator consists of two main components: a set of web pages providing a user interface to the software, and a set of MATLAB functions ('m-files') that check input data, carry out calculations, and return results (Balco et al., 2008). This function of ICE-D makes it a standalone application by allowing its users to provide new geochemical data and calculate exposure ages. The middle layer for exposure-dating, therefore, includes physical models for geographic and temporal variation in the production rate, numerical solution methods, geophysical and climatological data sets, physical constants measured in laboratory experiments, and calibration data (Balco, 2020). The observational data of sample locations, chemical composition, nuclide concentrations, and physical properties of the erratic boulder is used for the input data. In the transparent middle layer algorithms define a set of locally calibrated data such as: a set of production rate scaling models, paleomagnetic field reconstructions, nuclear interaction cross sections, and calibration data. The output of this provides approximate production rates for cosmogenic nuclides.

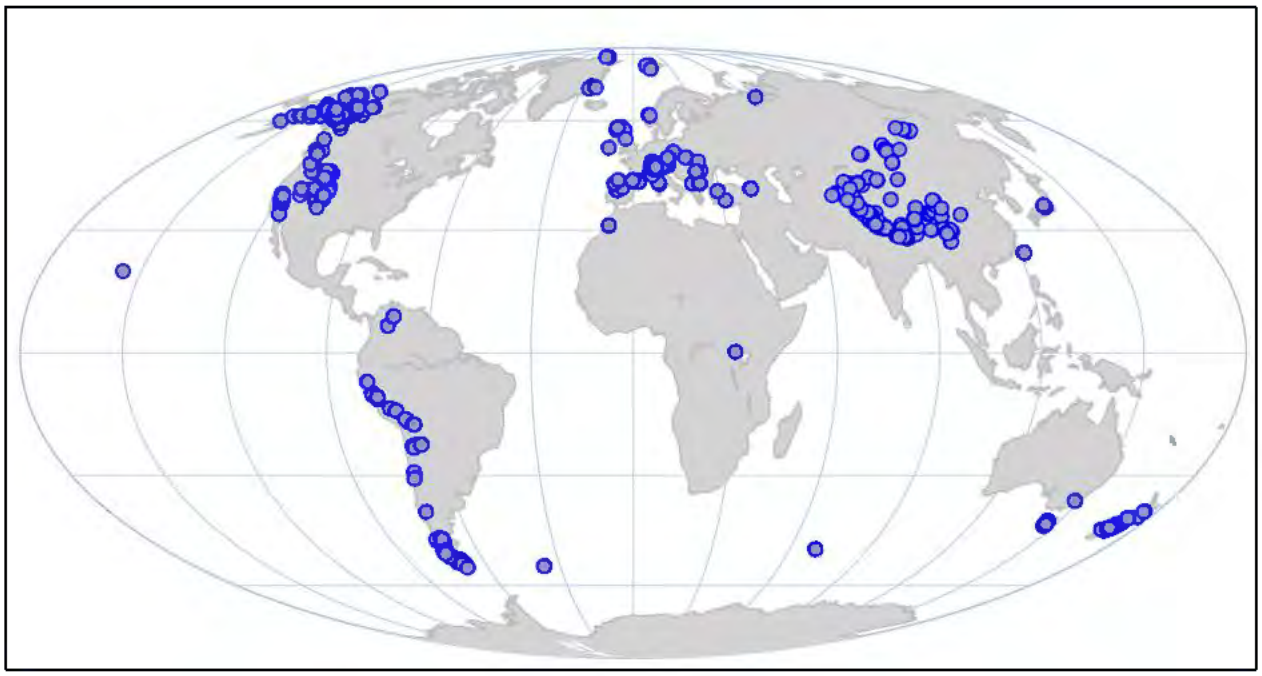

Figure 9. Spatial distributions of exposure dates found on ICE-D, where each dot signifies a glacial landform that has at least one exposure date, 2613 dots are included on this map. Representing a global chronology of glacial deposits distributed over space.

ICE-D allows users to access all published TCN exposure ages and geochemical data to incorporate in geoscience research. ICE-D provides users with access to data from more than one thousand unique glacial features in the conterminous U.S alone and over 400 TCN exposure ages of glacial features in the Great Basin (Fig. 10). ICE-D provides the data and calculations needed to evaluate the timing of Pleistocene glaciations in the Bonneville Basin, which has been developed through studies spanning the last two decades.

Figure 10. Zoomed in version of the interactive map found in the ICE-D website, http://ice-d.org displaying the plethora of cosmogenic nuclide exposure ages in the Great Basin. Ages of ranges discussed in this analysis can be obtained for the Ruby, South Snake, Deep Creek, Wasatch, and Uinta Mountains. Each numbered square indicates the number of samples taken from each site.

3.3. Methods

Many studies have been done across the Great Basin to understand the timing of past glaciations in the region. The chronology of the Ruby and East Humboldt range (Laabs et al., 2013; Wesnousky et al., 2016) identify both lateral and terminal moraines that correspond to the last glaciation. Studies done in the Uinta Mountains (Laabs et al., 2009; Laabs and Munroe, 2006, 2018) have identified a plethora of terminal and down valley recessional moraines that correlate to the Angel Lake advance. Additionally, a great deal of work dating moraines in the Wasatch Range (Quirk et al., 2020; Laabs et al., 2009) has been conducted identifying deposits from the last Pleistocene glaciation.

New production rate modeling developed for ^{10}Be by Lifton et al. (2015, 2016) was used to calculate more precise TCN exposure ages. Using a calibrated production model based on measurements of ^{10}Be concentrations found in two well dated surfaces in Lake Bonneville (Laabs and Munroe, 2016). This provided an exceptional new production rate for moraines in the Great Basin because of the proximity to Lake Bonneville and the new precision needed to understand how glaciers formed during the last glaciation. Additionally, Lifton et al. (2014) presented a new, physical based model for scaling the production rate. This new model termed "LSD" (Lifton-Sato-Dunai) takes advantage of all available scaling models in a statical analysis of known and predicted ages. The scaling methods presents the most robust considerations on the effects of geomagnetic latitude, atmospheric depth, and time on the production of spallogenic and muonic production of ^{10}Be (Laabs and Munroe, 2016).

3.4. Results

3.4.1. Western Uinta Mountains

Laabs et al. (2009) identified two groups of exposure ages; an older group represented by terminal moraines in northern and eastern glacial valleys, and a younger group represented by terminal moraines in the southern and western valleys. Laabs and Munroe (2016) recalculated ages of several terminal moraines across the entire Uinta Mountains. On the western side, terminal moraines for East Fork Bear River and North Fork Provo River were samples for TCN exposure dating. On the easter side Smith Fork valley, Yellowstone River valley were samples for TCN exposure dating. Mean exposure ages obtained from terminal moraines in the East Fork Bear River and North Fork Provo yielded mean exposure ages of 19.0 ± 0.9 ka and 18.3 ± 1.5 ka. Lateral moraines in the Bear River (main valley) and North Fork Provo yielded mean exposure ages of 18.2 ± 0.9 ka and 18.0 ± 0.7 ka. Additionally, lateral moraines in Bear River suggest ice

was there before the end of the LGM 20.1 ± 2.2 ka. Ice retreat was seen earliest in the South Fork Ashley Creek, 21.4 ± 1.6 ka, on the eastern side of the Uinta Mountains.

3.4.2. Wasatch Mountains

Many previous studies have been done TCN dating moraines in the Wasatch Range (Laabs et al., 2011; Laabs and Munroe 2016; Quirk et al., 2018) and suggest that terminal moraines were deposited prior to the Lake Bonneville high stand. Quirk et al. (2020) reports sixty-three recalculated TCN exposure ages in the valleys Little Cottonwood, Big Cottonwood, American Fork, Bells and Dry Creek Canyon in the Wasatch Mountains. Terminal moraine ages for the Bells Canyon yielded the oldest of the moraines sampled with a mean TCN exposure age of 23.0 ± 1.2 ka. Little Cottonwood left lateral moraine yielded as exposure age of 20.8 ± 2.2 ka and Big Cottonwood Mill B left lateral moraine yielded a mean age of 20.9 ± 0.2 ka. Lastly, Dry Creek terminal moraine yielded the youngest exposure date of 19.6 ± 0.8 ka. The initial abandonment of terminal moraines in the Wasatch Range occurred sometime between 22-20 ka. The Wasatch exposure dates suggest that an initial glacial advance likely occurred early in the LGM and occupied maximum extents until 23.0. prior to the Lake Bonneville high stand.

3.4.3. Ruby and East Humboldt

The Ruby Mountains contains spectacular alpine glacial geomorphology, in valleys like Seitz and Hennen Canyon. Laabs et al. (2013) conducted TCN exposure dating for a terminal and six recessional moraines in the Seitz Canyon that correlate to the Angel Lake advance, a total of twenty-nine exposure age samples were taken from the seven moraines. The mean exposure age of the five sampled collected from the only terminal moraine in Laabs et al. (2013) yields an age of 20.9 ± 2.1 ka. The six recessional moraines sampled contain decreasing exposure ages starting with the Recessional 1 working sequentially to Recessional 6. Seven

samples were collected from Recessional 1, yielding a mean exposure age of 18.8 ± 2.0 ka. From the Recessional 2 moraine five samples were collected yielding a mean exposure age of 20.6 ± 1.4 ka. Four boulders were sampled on Recessional 3, yielding a mean exposure age of 16.9 ± 2.5 ka. Only two boulders were sampled on the Recessional 4 moraine that yielded a mean exposure age of 16.1 ± 1.0 ka. Comparatively, only two samples were collected from Recessional 5 yielding a mean exposure age of 15.5 ± 1.2 ka. Lastly, four samples were collected from Recessional 6 that yielded a mean exposure age of 15.2 ± 1.4 ka.

3.4.4. South Snake and Deep Creek

Laabs and Munroe (2016) recalculated exposure ages with updated production rates for ranges found in the Western Lake Bonneville Basin, Deep Creek, and South Snake range. Ages were obtained from two different terminal moraine complexes, where five samples were obtained from the Deep Creek Range and four samples were obtained from the South Snake range. In the South Snake range, the four samples taken originated from Dead Lake. The South Snake Range yielded a mean exposure age of 17.1± 2.4 ka after the removal of one outlier in the set. In the Deep Creek Range, the five samples taken from the terminal moraine complex originated in the Granite Creek. Exposure ages calculated for the Deep Creek range yield ages older than the Bonneville high stand, with a mean age of 19.1 ± 0.3 ka after the removal of two outliers with ages around 11.0 and 30.0 ka. The mean exposure age found in the South Snake are younger than the ones obtained from the Deep Creek Range. Ice in the Deep Creek Range occupied terminal moraines until 19.1 ka, suggesting glaciers began retreating prior to the overflowing phase of Lake Bonneville.

3.5. Discussion of Cosmogenic Chronology and Implications for Paleoclimate

Using TCN exposure dating in the Great Basin, the timing of deposition of terminal and down valley recessional moraines have been constrained. Based on the finding of TCN dating, most glaciers in the Great Basin reached their maxima from ~22.0-17.0 ka. taking place during the transgressive phase of Lake Bonneville (30.0 ka- 18.0 ka) which began prior to and ended after the LGM (26.5-19.0 ka). The average age of a terminal moraines in the Great Basin is 19.8 ka, calculated from terminal moraines in the Wasatch, Ruby, East Humboldt, South Snake, Deep Creek, and Uinta mountains. The timing of terminal moraine deposition in the Lake Bonneville Basin suggest that glaciers advanced to their maxima position prior to the high stand of Lake Bonneville. Suggesting that climate following the LGM favored the expansion of alpine glacier, but not the expansion of Lake Bonneville.

Down valley recessional moraines in the ranges previously listed were deposited from ~18.0-15.0 ka (Fig.11) with a region average deposition age of 15.4 ka. This suggests that glaciers in the Great Basin left their terminal positions and began to retreat prior to or during the occupation of the Provo shoreline ~18-15 ka, while Lake Bonneville overflowed. The fact that glaciers reached their maxima before Lake Bonneville reached its high stand suggests that the latter part of the LGM was cold and dry, favoring the culmination of glacier maxima while lakes were below their high stand elevations, followed by a transition to a wetter climate that favored the maxima of both glaciers and lakes. The work of Quirk et al. (2020) on lake and glacier reconstructions in the Wasatch Range supports the finding that after the LGM there was an increase in effective moisture in the region. He suggests that both, an increase in precipitation and, a gradually increase in temperatures would have been needed. Conversely Belanger et al. (2021) suggests that glacier maxima during the LGM was not caused by larger increased in

precipitation, but rather modern precipitation values were combined with temperature depressions creating a positive hydrological budget. Although the uncertainties that surround TCN dating have been greatly reduced over the last decade, TCN investigations of glacial moraines alone do not provide enough information on magnitude and timing of climate change in the Great Basin to be used as a climate proxies. The effect Lake Bonneville had on glacier maxima and the effective precipitation in this region and moreover, on paleoclimate is inspected further in the next section.

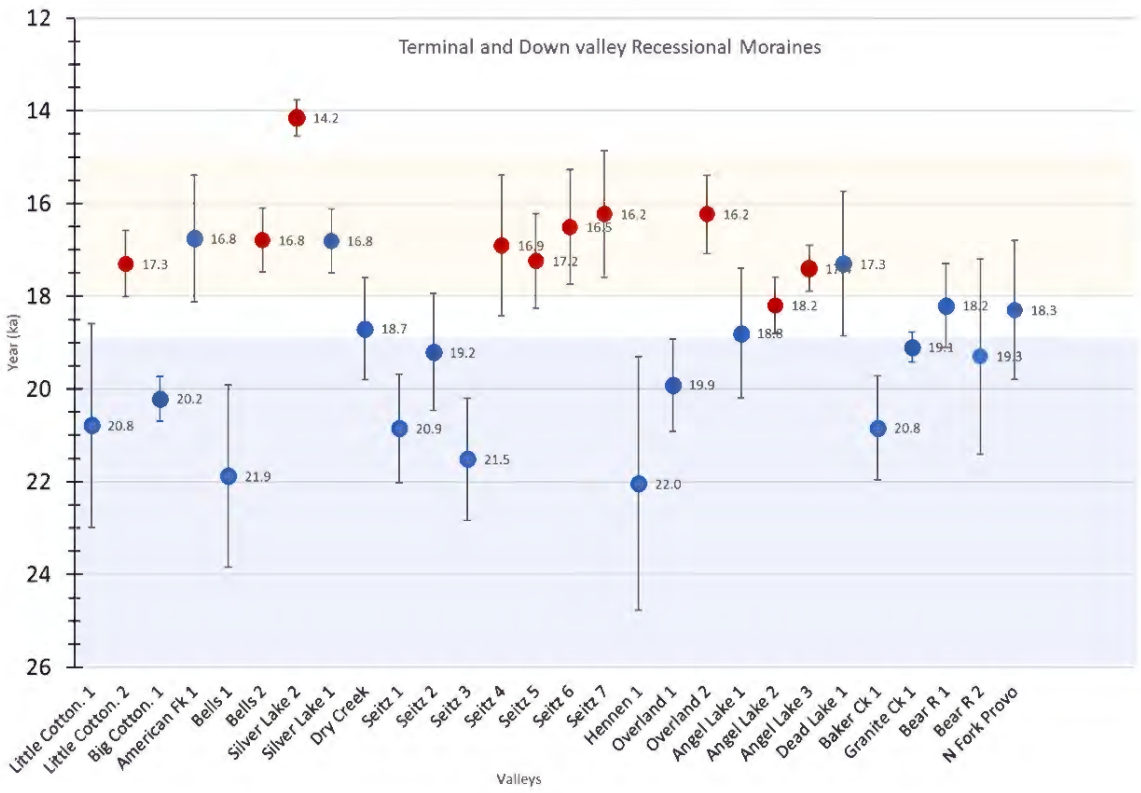

Figure 11. Terminal moraines, show as blue dots and recessional moraines shown as red dots, in the Bonneville Basin are compared to the timing of the LGM (26.5-19.0 ka), shown as a blue box and Lake Bonneville's overflowing shoreline (18.0-15.0 ka), shown as a yellow box. Recessional moraines in the Great Basin were occupied by valley glaciers during the overflowing stage of Lake Bonneville.

4. PALEOGLACIER AND ELA RECONSTRUCTIONS

4.1. Introduction

In this thesis, a set of numerical tools for reconstructing paleoglacier surfaces and ELAs (Pellitero et al., 2015; 2016) is applied to nine mountain ranges in the northeast Great Basin, all situated near or within the Lake Bonneville Basin in Utah and Nevada; the Ruby, Independence, East Humboldt, South Snake, Oquirrh, Deep Creek, Stanbury, Wasatch and Uinta Mountains to evaluate the spatial pattern of the last glaciation and infer paleoclimate based on ELAs. Pellitero et al. (2015, 2016) developed a set of spatial analysis tools for glacier and paleoglacier analysis within a geographic information system (GIS). The set of tools are scripted in Python 2.7 and use arcpy (ESRI toolset for Python), os, numpy and operator libraries. These tools present a unique method for reconstructing paleo glacier surfaces and ELAs based on glacial geomorphology. The tools are especially useful in the Bonneville Basin, where previous mapping studies and outlines of paleoglacier (Munroe and Laabs, 2009; Laabs et al., 2011; 2013; Quirk et al., 2018) provide the framework for testing a new set of tools on a large number of paleoglaciers (n = 263).

The first set of tools presented by Pellitero et al. (2016), abbreviated GlaRe, Glacier Reconstruction, contains 5 different methods for creating the equilibrium shape and thickness of a paleoglacier. Each tool requires inputting a different characteristic of the paleoglacier needed to recreate its surface, such as sheer stress, bed elevation, a shape factor (F), and trunk stem. The numerical approach applies equations of glacier motion from Nye (1952a, b) to create a glacier equilibrium profile. This approach assumes the following; (1) the present-day topography is the same as the paleo glacier topography and has undergo little erosion, (2) the reconstructed glacier was in equilibrium with its climate, (3) the paleoglacier was not a water terminating glacier, i.e., there was no calving on the ice margin (which was true for all paleoglaciers in the Bonneville

Basin) (Pellitero et al., 2016). Additionally, the tool does not take into account the effects of basal sliding on ice thickness and assumes that ice has a perfect plasticity rheology, that is, the glacier surface profile reflects flow chiefly by internal deformation of glacier ice (Benn and Hulton, 2010). The tool requires three different user inputs, basal shear stress, shape factor and the interpolation procedure.

The second tool used in this analysis by Pellitero et al. (2015) is a set of tools for calculating a glacier ELA based on its surface elevation. The tools permit calculating ELAs based on several different methods; however, for most situations, the most accurate are the physically based calculations of ELA using the Area-Accumulation Ratio (AAR) and Area-Accumulation Balance Ratio (AABR) methods, based on the well-known relationship between glacier hypsometry and mass balance. The AABR method assumes that the accumulation and ablation gradients are approximately linear, the net ratio between ablation and accumulation is known and remains fixed while the glacier occupies a moraine, and that the topography constraining the glacier is represented by the terminal moraine. The AABR method recognizes that any unit on the glacier surface that is altitudinally further away from the ELA has a greater contribution to the overall mass balance of the glacier (Pellitero et al., 2015). The AAR method for ELA reconstruction requires well-preserved geomorphic features to delimit the area covered by a glacier and is bested applied to glaciers that contain a relatively simple distribution of area-altitude (Munroe and Mickelson, 2002). Once the area has been outlined, the assumed AAR is used to subdivide the glacier area into an accumulation and ablation zone, with the ELA forming the boundary between them. Therefore, the AABR method accounts for the change in mass balance along the glacier surface, unlike the AAR method. A crucial step of this method accounts for the differences between the accumulation and ablation gradients with respect to

their contribution to the overall mass balance. This can be calculated by the following equation (from Furbish and Andrews, 1984).

$$BR = \frac{\bar{Z}_{ac} A_{ac}}{\bar{Z}_{ab}\, A_{ab}} \quad \text{(Eq.1)}$$

Where:

Z_{ac} refers to the area-weighted mean altitude of the accumulation area, Z_{ab} refers to the area-weighted mean altitude of the ablation area. A_{ac} refers to the area of accumulation and A_{ab} refers to the area of ablation (Rea, 2009).

A simpler method for ELA calculation, Median Glacier Elevation (MGE) is presented in Pellitero et al. (2015), where mass balance is a linear function of altitude, and the ELA is situated on the median glacier elevation. The AABR method for calculating paleo-ELAs was applied to glacial valleys across the Bonneville Basin. The AABR calculation is recognized to be more robust than the AAR and MGE methods because it accounts for both the glacier hypsometry and the mass balance gradients (Rea, 2009; Pellitero et al., 2016).

4.2. Previous ELA Calculation Methods

Munroe and Mickelson (2002) calculated ELAs for nineteen northern Uinta glacial valleys based on glacial landforms such as lateral and end moraines to reconstruct paleoglacier shapes. Munroe and Mickelson (2002) present four different methods for calculating ELAs: AAR, THAR, LM, and CIR. The AAR calculation does not provide any knowledge of mass-balance gradients in the calculation, only the shapes of the glaciers are taken into consideration in the calculation, not the surface. AAR relies on the assumption that accumulation-area to total-area ratio of 0.50-0.65 when in equilibrium with its climate (Meierding, 1982). Without the balance ratio calculation, those methods are at a disadvantage to the AABR method, because they neglect the physical attributes of a glacier such as basal shear stress and therefore, assumes

the ice thickness and slope. Without the contribution of the balance ratio to a method, only a theoretical shape for the glacier can be derived from geomorphology.

Comparatively, the THAR method for ELA calculation also takes into consideration the glacial geomorphology, but without consideration of paleoglacier shape. The THAR method relies on the assumption that ELAs on modern glaciers are located at an elevation that is equivalent to 35-40% of the total elevation difference between the terminus and the top of the glacier (Munroe and Mickelson, 2002). This is based on the observations of Meierding (1982), who observed toe-to-headwall altitude ratios for modern glaciers and found that a THAR of 0.35-0.40 most accurately predicted the ELA. However, Meierding (1982) concluded that the AAR method incorporates the physical attributes of the glacier surface better than that of the THAR method, because it integrates surface areas and absolute elevations, whereas the THAR methods consider two elevations (Meierding, 1982).

The third method for ELA calculations, abbreviated LM, presented by Munroe and Mickelson (2002) involves examining the maximum altitude of lateral moraines in glaciated valleys. For glaciers in steady state with their local climate, ice flows away from the margins in the accumulation zone and flows toward the ablation zone, therefore, the creation of lateral moraines occurs in the ablation zone. Thus, the highest elevation along a lateral moraine should coincide with the ELA (Munroe and Mickelson, 2002). Due to postglacial erosion and removal of lateral moraines, this method may underestimate the ELA. Additionally, the LM method poses further issues in determining the maximum elevation of lateral till. For example, bedrock ridges and other alpine landforms can be mistaken in some environments for lateral moraines. For these reasons, maximum lateral moraine altitude remains one of the least reliable methods for ELA

determination. However, for glacial valleys where terminal moraines are not preserved, the LM method could yield the most accurate results.

A final method for calculating ELAs used by Munroe and Mickelson (2002) is the cirque floor elevation method (CIR). Cirque floors can represent the lowest elevation of downward glacier flow and attendant erosion of the valley floor and, therefore, can provide an estimate of the lowest elevation of the accumulation zone. Cirque floor elevations contain similar aspects correlated to ELAs and therefore, yield an estimate of the ELA (Munroe and Mickelson, 2002). However, the CIR method presents its own set of potential errors due to postglacial erosion from multiple glaciations. The CIR method provides the lower limit of the cirque formation but provides no upper limit other than that cause by the topography. Additionally, cirques that are positioned at the low end of their altitudinal range are more difficult to identify than higher altitude cirques because they are occupied by thinner ice for a shorter time (Meierding, 1982). Due to the many subjective decisions that influence the derived ELA, such as high natural variability of cirque-floor altitudes render this the most unreliable ELA method.

4.3. Methods

4.3.1. Application of the GlaRe Tools

A subset of the GlaRe tools was developed within a GIS and applied to all glacial valleys in the Bonneville Basin. The flow diagram for the GlaRe tool applied here (Fig. 12) follows the simplest central path; where parameters are depicted as blue circles, tools are assigned to a yellow box and tool outputs are shown as green circles. Of the five tools described in Pellitero et al. (2016), two are utilized for this analysis, Flowline Ice Thickness tool and the Glacier Surface Interpolation tool. These two tools were employed based on the known geomorphological characteristics of the valley. The inputs required for the tools used in this analysis are as follows;

digitized flowlines of the paleoglacier and its tributaries, digitized watershed, digitized paleoglacier extents and a digital elevation model (DEM) of the glacier. The tools used in this analysis were selected based on the different combination of inputs previously listed (Pellitero et al., 2016). For this study, terminal moraines corresponding to LGM ice extents, in mountains with TCN exposure ages of moraines, have been digitized in GIS to delimit glacier outlines. Flowlines and watersheds were digitized in ArcGIS Pro based using topographic maps and paleoglacier outlines as digitized polygons. Paleoglacier outlines were obtained from mapping of Munroe and Laabs (2009), Laabs et al. (2011), and Laabs and Munroe (2016).

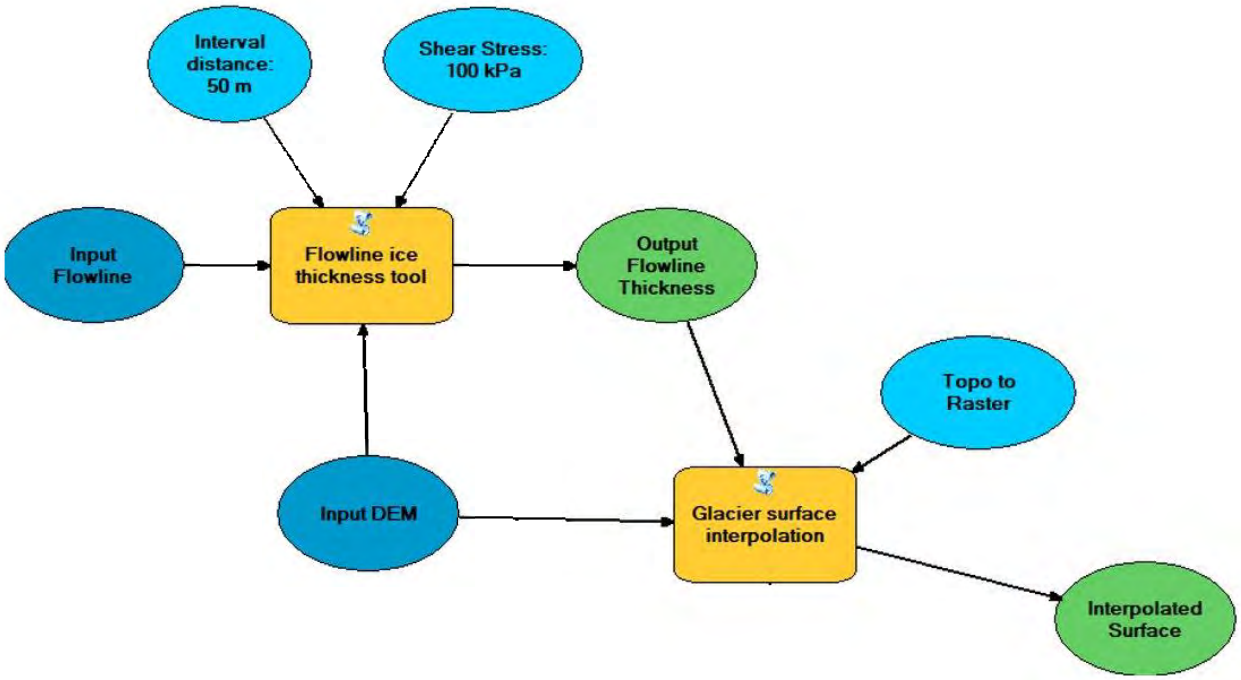

Figure 12. Schematic flow for the GlaRe tool, where dark blue circles define user inputs, yellow boxes define tools presented in (Pellitero et al., 2016), light blue circles define user parameters, and green circles are tool outputs. The GlaRe tool takes geomorphological inputs of the glacier to reconstruction the paleo-glacier surface.

The first tool executed in the GlaRe toolset is the flowline ice thickness tool that constructs a thickness profile of the glacier based on (1) digitized flowlines which define the paleoglacier hydrology, (2) a DEM clipped to the watershed of the glacial valley, (3) an assumed

glacier basal shear stress value of 100 kPa, (4) and a contour interval of 50 m. The relationship of basal shear stress and flow by internal deformation of a glacier is defined by Glenn's flow law (Bennett and Glasser. 2013), with shear stress directly proportional to the thickness, slope angle of the glacier surface. The assumed shear stress of 100 kPa primarily determines the thickness and slope of the computed glacier surface. Pellitero et al. (2016) performed tool testing to identify which scenario of inputs creates the most accurate output surface and volume. They found that without the use of the shape factor tool, which relates the cross-sectional area and perimeter length, the volume of the glacier is underestimated by 25-30% (Pellitero et al., 2016). However, they discuss that this problem can be easily overcome through a denser flowline pattern. For this reason, I digitized all flowlines within trunk valleys and tributaries of the modern glacial valley, extending from the terminal moraine to cirque headwalls. Through the work of Laabs et al. (2011), precise glacier limits were delimited allowing for the clipping of features (flowlines and the watershed) to the mapped terminal moraines. Without the correct identification of terminal moraines, the tool would exhibit error in the horizontal geometry of the glacier reconstruction (Pellitero et al., 2016).

The output of the flowline thickness tool provides the input for the surface interpolation tool in the GlaRe toolset, along with the clipped DEM. The surface interpolation tool includes options for interpolating the glacier surface. Four different interpolation methods were tested, Topo to Raster, Inverse Weighted Distance (IDW), Kriging, and Trend. This step is instrumental in obtaining an accurate paleoglacier because the tool converts the 2D ice thickness flowline into a 3D surface representing the thickness and topography of the paleoglacier. The Topo to Raster method performs a set of 20 iterations, which calculates grids at progressively finer scales. The more iterations performed the smoother and more continuous output surface is achieved. One

assumption made when calculating the ice thickness profile, is the tool assumes that the glacier flowline edges intersect the DEM at the same elevation across the ice surface. Creating a hydrologically correct surface, however, possibly underestimating a few meters of ice. This method of interpolation produced glacier shapes and thickness consistent with glacial mapping in valleys in the Bonneville Basin and was used for all glacier reconstructions in this study. Glacier reconstruction is necessary for the calculation of paleo-glacier ELAs and subsequent derivation of quantitative paleoclimatic data (Pellitero et al., 2016).

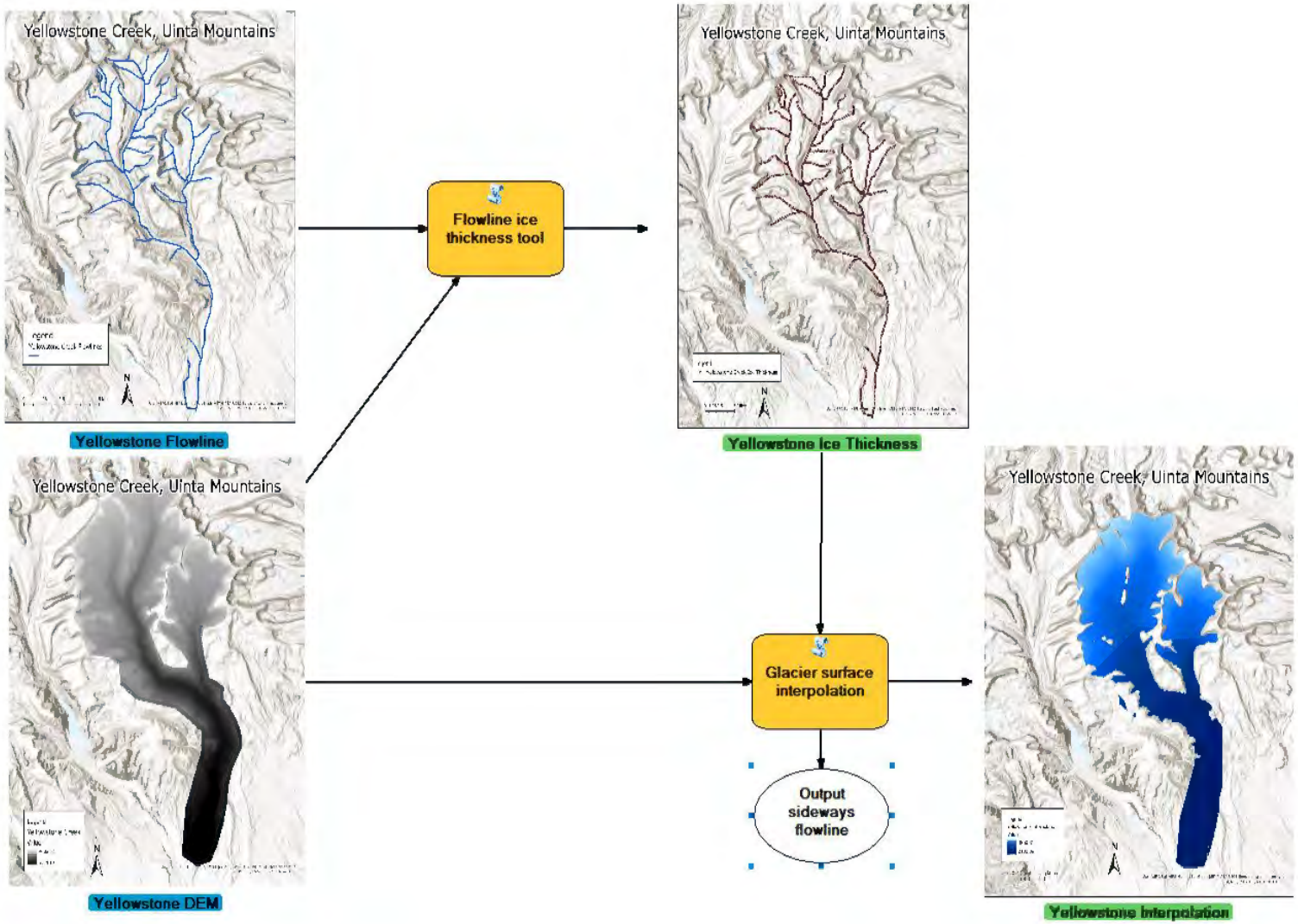

Figure 13. Schematic flow for the GlaRe tool, with illustrations of input and output layers.

4.3.2. ELA Reconstruction

Calculating an ELA based on AABR methods, as discussed above, relies partly on the observation that modern glaciers contain an accumulation-area to total-area ratio of 0.50-0.65 when in equilibrium (Meierding, 1982). For this analysis, an accumulation-area ratio of 0.65 was used as the accumulation area because it is observed for most modern land-terminating mountain glaciers (Meierding, 1982). The AABR calculation is implemented in two steps, the first step defines the distribution of surface area with regards to elevation, this is done by dividing the glacier into belts bounded by 50 m surface contours. Default contour belt values provide by the tool are defined as 50 m and was the contour interval used in this analysis. For each belt, the area is multiplied by the mid-point of the elevation, and values are then summed and divided by the total area of the glacier (Pellitero et al., 2015). The second step of the calculation accounts for the balance ratio of the glacier. This is done by testing iterations of multiple paleo glacier mass balances for all possible ELAs, starting at the mid-point of the lowest contour belt. For each iteration, the trail ELA is subtracted from the mean count our belt altitudes and then multiplied by the contour belt area (Pellitero et al., 2015). The result is either a positive or negative number that represents the net mass balance. Iterations are repeated until the contour belt where the net mass balance changes from positive to negative. Computational speed determined by contour interval, which is user defined, and the glacier size. The parameters required to run the calculation consists of a Digital Elevation Model (DEM) and the ratio for the AAR and AABR methods. Reconstructing the 3D geometry and ELAs of paleo glaciers is an essential part of understanding how temperature and precipitation functioned during the Late Pleistocene.

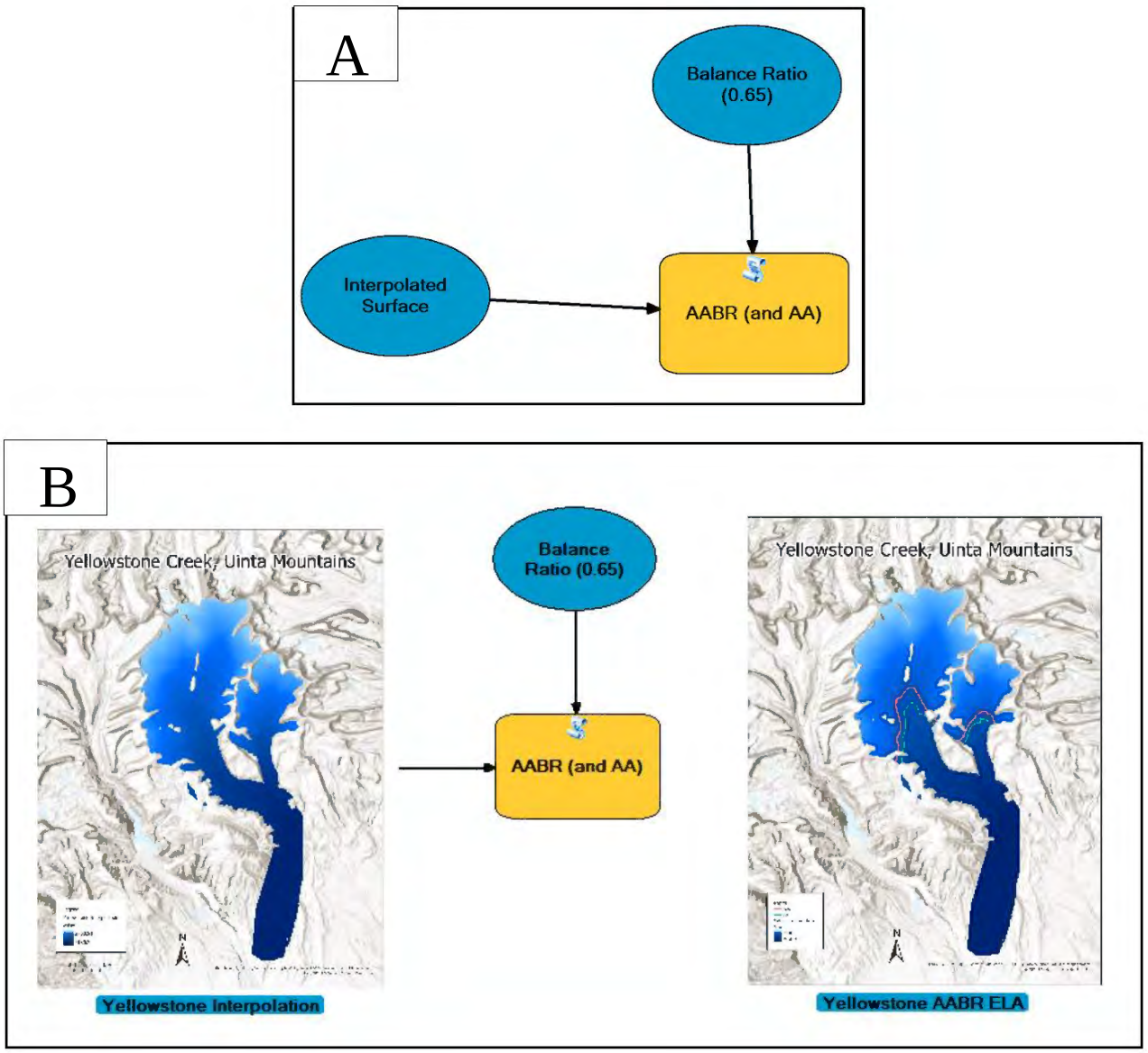

Figure 14. (A) Schematic flow for the ELA tool, where blue circles define user inputs, yellow boxes define tools presented in (Pellitero et al., 2016). Inputs are derived from the GlaRe tool and user defined area-accumulation ratio of 0.65. The output is an ELA calculation. (B) Schematic flow for the ELA with illustrations of surface from the GlaRe tool and the output ELAs.

4.3.3. Volume Calculation

The reconstruction of paleoglaciers in the northeastern Great Basin afforded new and more precise calculations of ice surface area and volume, which were previously estimated for a small number of glaciers in the study area using area-volume scaling relationships (Laabs and

Munroe, 2016). In the GIS setting glacier surfaces for each range were combined into one layer raster layer. Next, the thickness of the raster layer was obtained by subtracting a DEM surface from the new raster layer. Then, an interpolation method (Extract by Mask) was applied to the thickness layer and each cell of the raster layer was quantified. Lastly, surface area and volume were calculated in GIS where the area and volume between the raster layer and reference plane were calculated. Where the interpolated surface was used as the reference plane and the area below the plane was tabulated.

4.4. Results

4.4.1. Paleo-glacier and ELA Reconstructions

This thesis presents the first 3D reconstruction of paleoglacier surfaces and ELAs in the representing the LGM in the Lake Bonneville Basin/northeastern Great Basin. A total of 263 glacier surfaces were reconstructed across the region. In the Ruby Mountains, a total of ninety-two glacier surfaces were calculated making up the largest collection in this analysis (Fig. 5). Just north of the Ruby Mountains, twenty-four glacier surfaces were computed for the East Humboldt Mountains and thirteen surfaces were computed for the Independence Mountains. 100 km South of the Ruby Mountains by the Nevada/Utah boarder, ten glacier surfaces were computed for the South Snake Range ten surfaces were created. For a total 139 3D modeled glacier surfaces in Nevada. In Utah, seventeen glacier surfaces were reconstructed across small ranges near the area occupied by Lake Bonneville. From the Oquirrh range four surfaces were created, in the Deep Creek range five surfaces were created, and in the Stansbury range eight glacier were created. On the east side of Lake Bonneville, two ranges surfaces were recreated, in the Wasatch Mountains 50 valley glaciers 3D surfaces were reconstructed along with forty-six in the Uinta Mountains.

Table 1. Paleo ELAs in the Great Basin.

Mountain Range	Average AABR	AABR St. Dev	Average AAR
Independence	2604	78	2490
Ruby Mountains	2801	278	2680
East Humboldt	2712	113	2680
Stansbury	2684	100	2700
Deep Creek	3070	179	2890
Wasatch	2686	73	2420
Uinta	3131	231	2940
South Snake	3067	70	N/A
Oquirrh	2753	153	2660

Note. Comparison of the average ELAs derived in this study vs. the average ELAs obtained in the map-based calculations in Laabs and Munroe (2016).

Glaciers to the west of Lake Bonneville in Nevada: Ruby, East Humboldt, South Snake, and Independence Mountains combined had a total ice volume of 106 km^3. Glaciers nearer to the lake in the Oquirrh, Deep Creek, and Stansbury Ranges were much smaller, glaciers with twenty-seven glaciers yielding a total ice volume less than 1 km^3. On the east side of the area that occupied by Lake Bonneville ice volumes were calculated for the Wasatch, Uinta, and the western Uinta Icefield. Glacial valleys to the west of the Provo River in the Uinta Mountains constituted 299 km^3 of ice volume, and the total ice volume held by the Uinta Mountains was 573 km^3. Calculated ice volume in the Wasatch Range reached 36 km^3 during its LGM extents. Therefore, the recalculated volume for the western Uinta icefield (Wasatch Range and valleys west of the Provo River) is 335 km^3. In the Bonneville Basin volumes were tabulated to yield a total volume of 304 km^3 and the total ice volume calculated for all 263 glacial valleys in this analysis was 2 km^3.

Table 2. Ice Volume Calculations for Glacier Reconstructions.

Mountain Range	Area (km^2)	Volume (km^3)
Eastern Uinta	2685	573
Western Uinta	789	299
Ruby/Independence/East Humboldt	340	106
Wasatch	238	36
South Snake	30	3
Stansbury/Oquirrh/Deep Creek	<1	<1
Total NE Great Basin	4083	1018
Total Bonneville Basin	1397	444

Note. Volume and Area calculations achieved using the output glacier reconstructions from the GlaRe tool.

4.5. Discussion

All ELAs calculated here using the AABR method described above are 12-200 m higher than the map based ELAs determined in Laabs and Munroe (2016) (Fig. 16). The Stansbury Range yielded the smallest difference in average ELA of 12m compared to map-based reconstructions of Laabs and Munroe (2016). The Wasatch Range yielded the greatest difference of 200 m compared to map-based reconstructions; however, this could be attributed to the greater number of reconstructed glaciers and ELAs in this study (n=50) compared to Laabs and Munroe (2016) (n=5). When comparing the five ELAs in Laabs and Munroe (2016) against the same five valleys in this analysis an average of 2642 m is achieved for the AAR method and an average of 2789 m is achieved for the AABR method. This demonstrates a systematic change in the two different methods for calculating ELAs. For ranges with similar sample sizes to Laabs and Munroe (2016), the Deep Creek range yielded the most change of 180 m. One reason ELAs in this analysis are higher than the ones found in Laabs and Munroe (2016) is because the method used for calculating ELAs Laabs and Munroe (2016) used the AAR method for ELA calculation. ELAs in this study are expected to be a more accurate representation of ELAs during the LGM

for a few reasons. First, the AAR calculations are hypothesized to underestimate the size for the glacier and the impact the balance ratio has on the ELA. Map-based calculations, like the ones used by Laabs and Munroe (2016), rely on a the planimetric area of a paleoglacier (as a polygon) to calculate the ELA, whereas the AABR methods used here utilize the reconstructed glacier surface area and mass balance gradient to calculate the ELA.

Although ELAs reconstructed here differ from the map-based reconstruction as described above, they follow the same overall general trend found in Laabs and Munroe, (2016), gradually increasing ELAs across the Great Basin from west-east, in Nevada, the gradually decreasing from west-east in the area around Lake Bonneville, and then rising sharply across the Uinta Mountains, the east/downwind side of Lake Bonneville (Fig. 16). An explanation for the west-east rise of ELAs across Nevada is the increasing distance from the Pacific Ocean, the primary moisture source for the Great Basin. The drop in ELAs across Lake Bonneville in Ranges such as Deep Creek, Stansbury, Oquirrh and the south-western side of the Wasatch (Fig. 17), are a result of the local moisture being derived from the Lake. Additionally, the rise in ELAs across the Uinta Mountains is a result of the increasing distance from the Lake, and the subsequent decline in moisture the further away from the Lake.

ELAs in the south-western Wasatch Mountains were the lowest found in the Lake Bonneville Basin, including glacial valleys Bunnell (2390 m), Big Spring (2398) and Tibble (2404 m). This pattern is not consistent with the distribution of modern precipitation. However, if temperature depressions relative to modern was a uniform function of latitude across the Great Basin at the start of the Lake Bonneville high stand ~18.0 ka, then precipitation patterns likely differed from modern (Laabs and Munroe, 2016). Winter precipitation is greater in ranges west

of the Wasatch but ELAs are found to be higher the Ruby/East Humboldt and Independence Mountains (2797 m asl) than the Wasatch (2686 m asl).

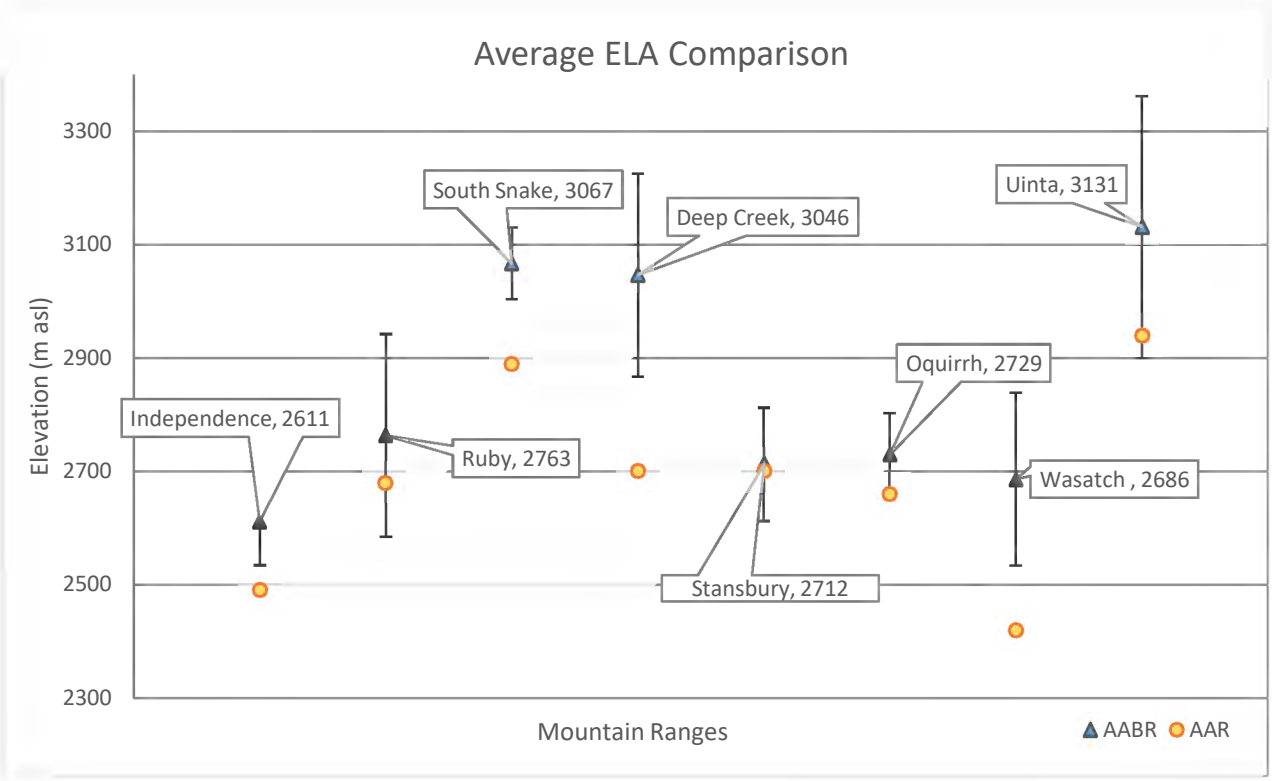

Figure 15. Average ELAs derived in this study vs. ELAs found in and Laabs and Munroe (2016). Yellow squares represent ELAs computed in this study using AABR methods of Pellitero et al., (2015, 2016) toolboxes in the GIS setting. Blue squares represented ELAs determined using AAR methods based on mapping (Laabs and Munroe, 2016). All ELAs derived in this thesis are higher than map-based calculations. The sample sizes for AABR methods: Independence (n=13), Ruby (n=92), East Humboldt (n=24), South Snake (n=10), Deep Creek (n=5), Stansbury (n=8), Oquirrh (n=4), Wasatch (n=50), and Uinta (n=46). Sample values for the AAR method: Independence (n=13), Ruby (n=116), East Humboldt (n=21), South Snake (n=10), Deep Creek (n=5), Stansbury (n=8), Oquirrh (n=4), Wasatch (n=5), and Uinta (n=46).

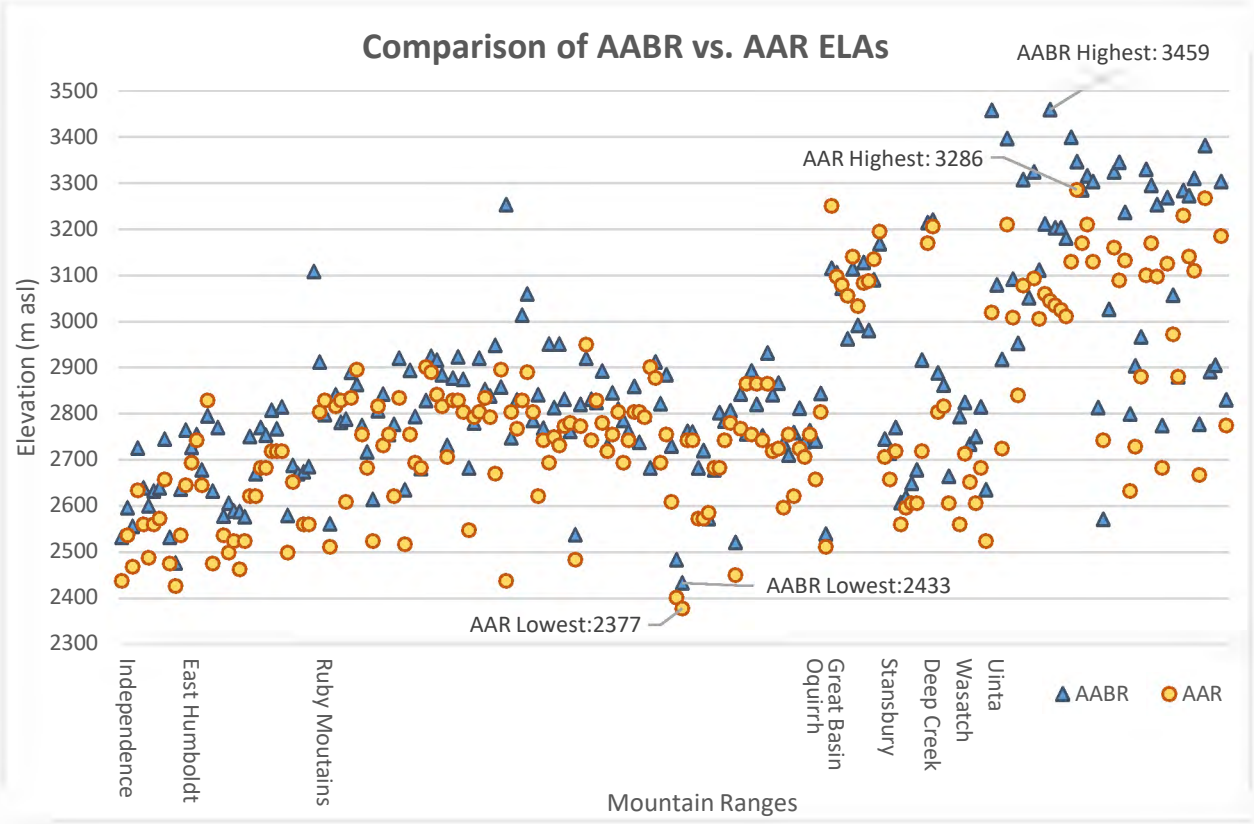

Figure 16. Markers on the graph represent ELA derived in Laabs and Munroe (2016) shown as yellow circles, and ELAs obtained in this analysis are shown as blue triangles. ELAs are arranged from west to east on the X axis and exhibit a slight decline in ELAs across the lake indicating and then a steep incline on the downwind side of Lake Bonneville.

Additionally, ELA trends across the Uinta Mountains derived in this analysis are concurrent with the trends found in Laabs and Munroe, (2016). This thesis further supports the interpretation of Munroe and Mickelson, (2002) of increased precipitation on the western side of the Uinta Mountains due to the presence of Lake Bonneville (Fig 17 A, B). ELAs on the west side of Bear River show a steep increase in ELAs over a relatively short distance. ELAs rise nearly 800 meters from west to east over a distance of 50 kilometers, confirming a difference in either temperature or precipitation on the east side of the Uinta Mountains. The difference across the Uinta's ELAs of over 800 m has been interpreted to reflect a decline in precipitation, too sharp to be attributed to orographic effects alone (Munroe and Mickelson, 2002; Laabs et al.,

2006; Laabs and Munroe, 2016). This is further supported by the presence of large, valley glaciers found in the western Uinta icefield and the small, discrete glaciers found on the east side of the Uinta Mountains.

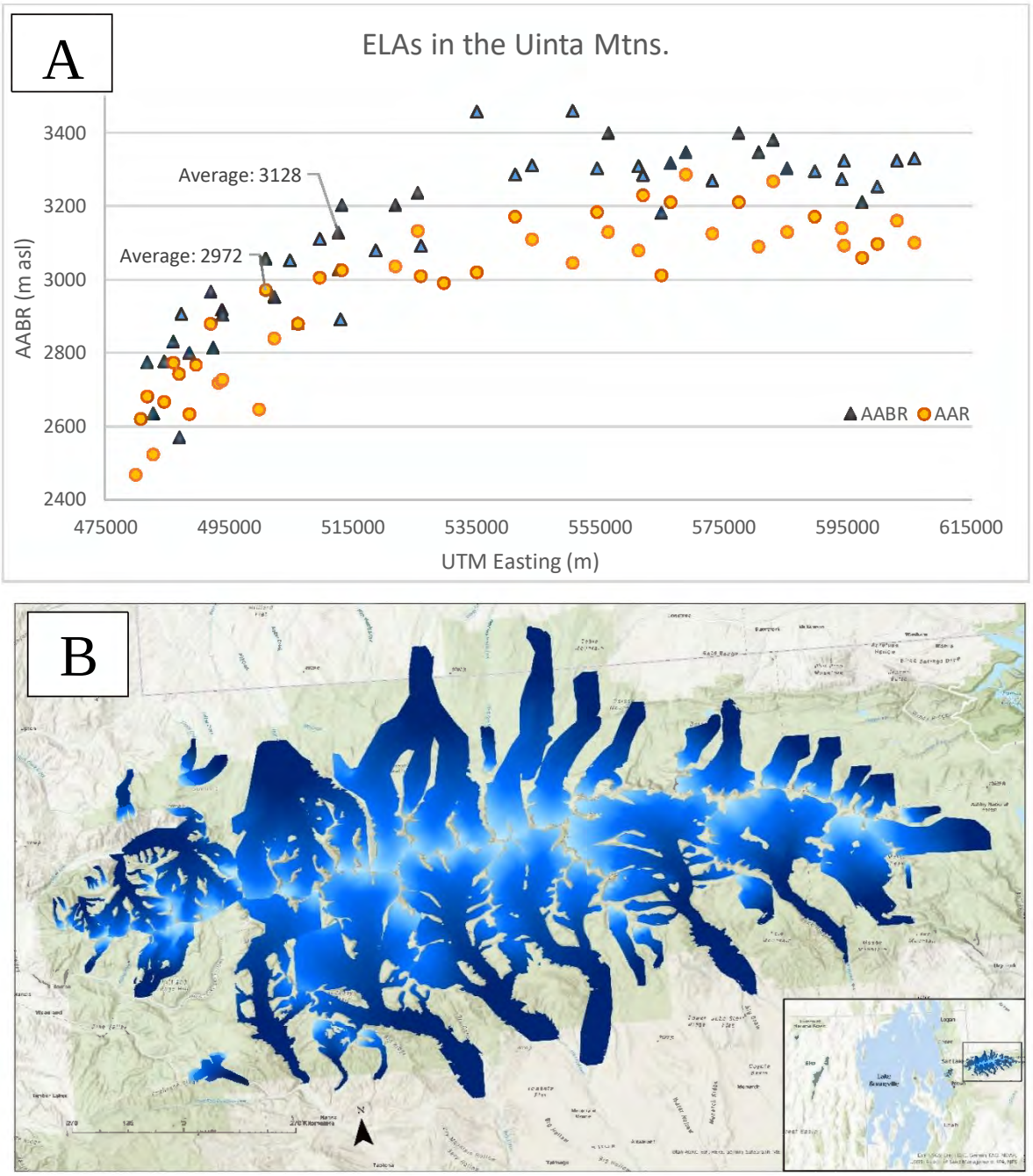

Figure 17. (A) Uinta ELAs achieved in this analysis are plotted against ELAs derived in Laabs and Munroe (2016) according to their easting positions. ELAs in the west show a decline in ELAs compared to the east side in both Laabs and Munroe results and the ones found in this thesis. (B) Glacier reconstructions created using the GlaRe tools in the Uinta mountains.

Mountains in Nevada to the west side of the area occupied by Lake Bonneville, exhibit large ELA variability within ranges and from north to south. The four ranges shown in (Fig. 18) are north to south trending ranges that span from the Independence to the South Snake Range, covering over 335 km. The overall trend of the ELAs show lower ELAs in northern glacial valleys and higher ELAs in southern valleys, with a total north-south difference of 800 m and high intra-range variability, especially in the Ruby Mountains. The increase in ELAs from north to south us likely due to the greater incoming solar radiation and surface temperatures for a given elevation at lower latitudes compared to higher latitudes. ELA variability within the Ruby Mountains alone account for an almost 700 m difference in ELA (Fig. 19). On the northern side of the Ruby Mountains, valleys like Secrets Peak East and West, Starvation Canyon and Robinson Creek had ELAs less than 2600 m. The lower in ELAs on the north side of the range could be attributed to increased precipitation on north facing valleys.

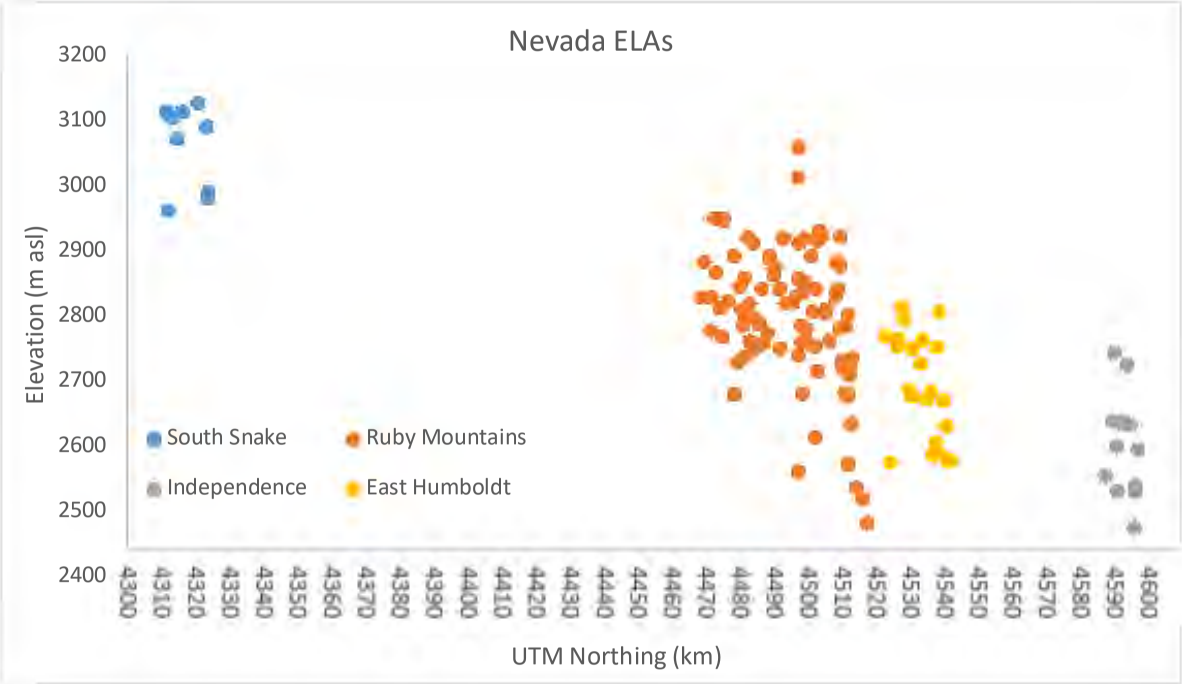

Figure 18. Variability in ELAs in the Ruby, East Humboldt, Independence, and South Snake ELAs with UTM northing. This graph displays the N to S trend of ELAs with respect to latitude, where the highest ELAs are found in the South Snake and the lowest ELAs are found in the Independence. As the latitude decreases, moving south, the ELAs begin to rise in elevation.

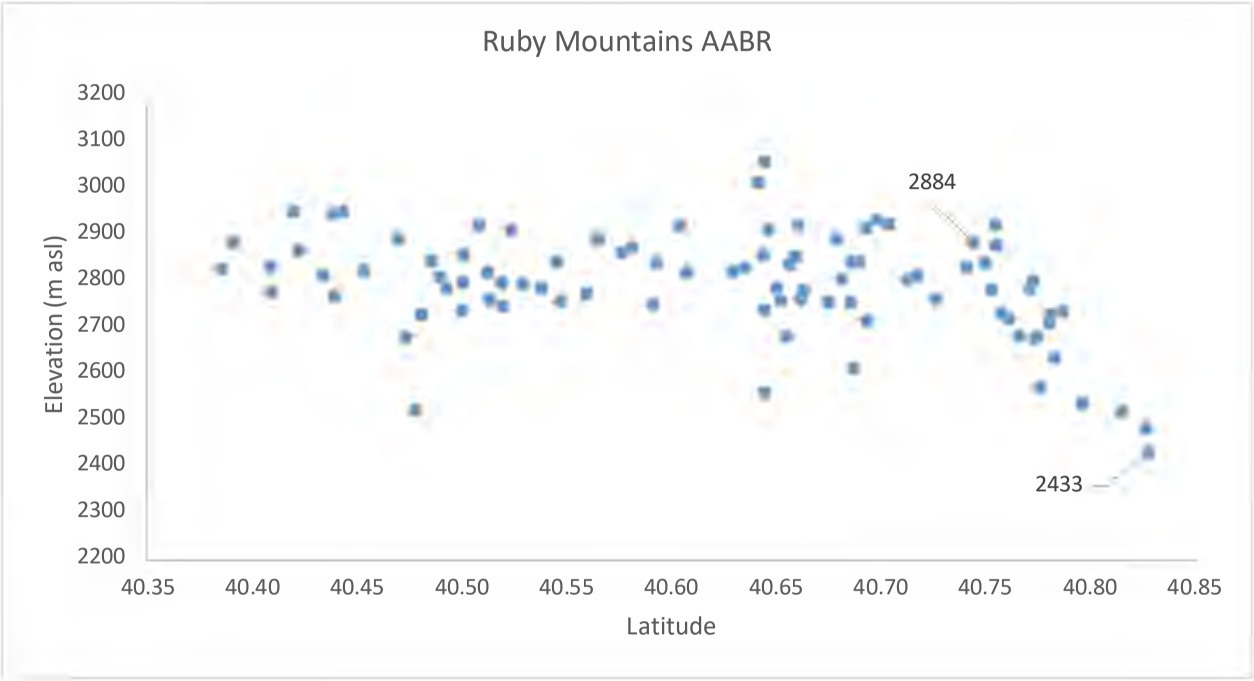

Figure 19. ELAs for the Ruby Mountains versus latitude. The graph displays a high level of variability, the lowest elevation of ELAs is 2433 m and the highest is 3060 m, these two points are just 50 km apart.

Lastly, updated ice volume calculations across the Great Basin and specifically in the western Uinta icefield reflect an underestimation of volume by Laabs and Munroe, (2016). The total ice volume calculated for the glacial valleys in this analysis constitute for 2254 km^3. The total ice volume calculated in this analysis for the western Uinta icefield (403 km^3) reflects an increase in volume of 156 km^3 when compared to the western Uinta icefield calculated by Laabs and Munroe, (2016) (247 km^2). Even with the addition of 162 km^3 to the total volume of the western Uinta icefield still only accounts for 4.9% of the total volume of Lake Bonneville (8603 km^3). These results suggest that glacial meltwater that may have originated in the western Uinta icefield during the LGM would not have been the driving factor in the Lake Bonneville overflow. This study refutes the notion that the total glacier volume in the Bonneville Basin made up a large part of the Lakes total lake volume. Suggesting a different source of moisture caused Lake Bonneville to overflow. Perhaps an increase in precipitation may have been the factor that controlled the overflow, this is discussed further in the next section.

4.5.1. Paleoclimate

Paleoglacier and ELA reconstructions in the Rocky Mountains by Leonard (2007) focused on quantifying the temperature and precipitation, during the LGM. Using methods from Ohmura et al. (1992), that summarized temperature and precipitation at modern glacier ELAs, Leonard (2007) assessed both temperature and precipitation changes from modern necessary to sustain glaciers during the LGM. This procedure was done using ArcGIS to identify pixels that would be above the ELA under a given set of input temperature and precipitation conditions (Leonard, 2007). Using Eq. (2) it was assumed that any pixel that satisfied the condition would be assumed to be in the accumulation zone.

Previous studies (Lowe, 1971; Sutherland, 1984; Leonard, 1989; Locke, 1989; Ohmura et al., 1992; Dahl et al., 1997; Zemp et al., 2007) define a non-linear relationship existing between accumulation/ precipitation and summer temperature at the glacier ELA. However, Leonard (2007) addresses a more complex relationship existing between glaciers, climate and the related ELAs. He makes the observation, from the work previously listed, that data obtained from glaciers with widely different climatic regimes did not retain a non-linear relationship, but instead an envelope of conditions. Leonard (2007) uses Ohmura et al. (1992) annual precipitation vs. summer temperature global relationship to further investigate the envelope of climate conditions during the LGM, in the Rocky Mountains. The global relationship is best described according to equation 2:

$$P_a = 19.543(T_s + 5.4)\ 2.0331 \qquad \text{(Eq. 2)}$$

Where P_a is the annual precipitation at the ELA and T_s in the mean 3-month summer temperature at the same location. Data from glaciers in North America positioned south of 52°N suggest a slight fall somewhat to the right of the best-fit line for Figure 18. The following equation (3) is revised from equation 2 to suffice the slight shift, signifying a 2.5° C temperature correction from the global model:

$$P_a = 19.543(T_s + 2.9)2.0331 \qquad \text{(Eq. 3)}$$

Eq. (3) assumes that 65 ±10% of the glacier area is above the ELA in the accumulation zone (Leonard, 2007). Temperature and precipitation models changed incrementally, and the area was defined by Eq. (3), once the area of pixels determined to be above the ELA account for 65% of the total area it is assumed that the modeled climate could sustain glaciers.

Using Eq. (2) and (3) curves for the ELA envelope (Fig. 17) were created to interpret the climate conditions needed to sustain glaciers maxima during the LGM. The same methods followed by Leonard (2007) for glaciers in the Rocky Mountains, was applied to ELAs in this

analysis. Modern temperature and precipitation values at the ELA were collected from gridded monthly average temperature and precipitation from the PRISM Climate Group, of Oregon State University (www.prism.oregonstate.edu). Values of modern temperature and precipitation were collected at the 263 ELAs and averages of each range were used to determine the modern temperature depression needed to sustain paleoglacier ELAs (Table 3).

Table 3. Modern Climate at Paleo ELAs in the Great Basin.

Mountain Range	Avg T* (° C)	Avg P* (mm)
Ruby Mountains	12	809
East Humboldt	12	874
Stansbury	13	1017
Deep Creek	12	745
Wasatch	14	969
Uinta	11	840
South Snake	13	703
Independence	13	903
Oquirrh	13	1062

Note. Modern average summer temperature (July-Sept.) and average yearly precipitation (Jan.-Dec.) at paleo ELAs derived from PRISM climate group data.

The average summer temperature and annual precipitation at the reconstructed ELAs vary across 3°C and ~300 mm precipitation (Table 3, Fig. 20), with the greatest temperature in the Wasatch Range and the lowest in the Uinta Mountains. Comparing the modern climate at the paleoglacier ELAs to climate at ELAs of modern glacier affords an opportunity to infer temperature and precipitation conditions during the LGM in the study areas. For example, a region-wide summer temperature depression of 10° C with no change in modern precipitation would have been needed to shift regional climate into the ELA climate envelope (Fig. 20). Alternately, with no change in modern temperature a 6-fold increase in modern annual precipitation is needed to shift modern ELAs into the climate envelope during the LGM. However, a 6-fold increase of annual precipitation compared to modern is likely not the

explanation for climate during the LGM. Because a colder climate than modern would have been needed to favored glacier maxima prior to the Lake Bonneville high stand. If there was an increase in annual precipitation during the LGM it would be expected that glacier maxima and the Lake Bonneville high stand would have occurred at the same time. The scenarios shown in (Fig. 20) are indicative of the possible climate variability experienced in the Bonneville Basin during the LGM. Additionally, because down valley recessional moraines are positioned just up valley from terminal moraines, we can make the assumption that glaciers would have been smaller and therefore, would have seen a rise in ELA elevation from terminal to down valley recessional positions.

Belanger et al (2021) through glacier and lake modeling found that from 21-20 ka Lake Bonneville was larger than it was at the Provo shoreline (18.0-15.0 ka) but had not yet reached its overflowing phase. Belanger (2021) work suggests that with a temperature depression of 9°C only a 7% increase in precipitation would be needed and that Lake Bonneville's level during the LGM was primarily driven by colder temperatures that suppressed evaporation. These conclusions are in agreement with glacier modeling studies by Quirk et al (2020) suggesting that near the end of the global LGM (21.0-20.0 ka) climate was primarily driven by a decrease in annual temperatures with little to no change in precipitation compared to modern. However, Belanger et al. (2021) and Quirk et al. (2020) analysis' only focus on a small number of glacial valleys in the Wasatch Range. Whereas this analysis contains ELAs across the entire Bonneville Basin and covers a large quantity of glacial valleys in the Great Basin.

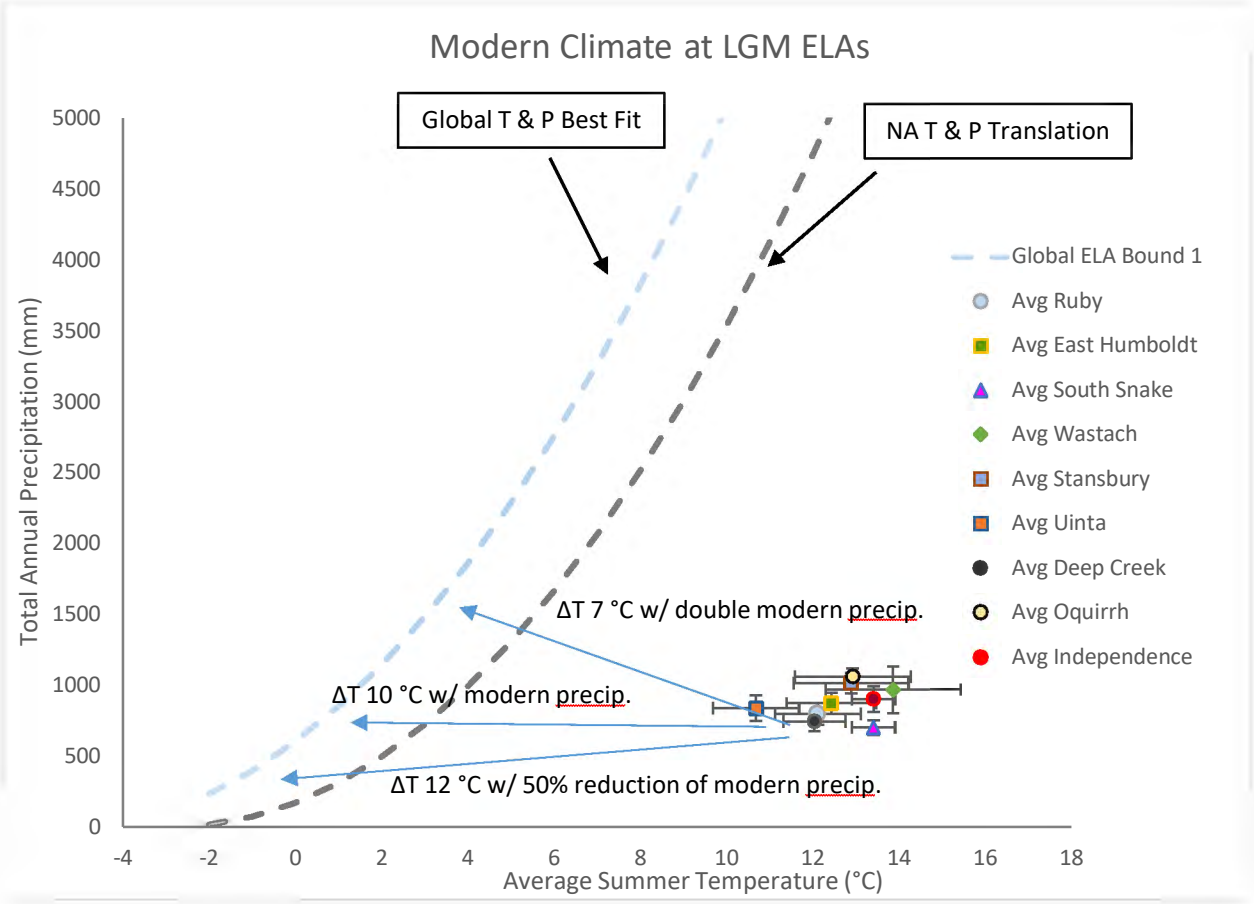

Figure 20. Modern climate at LGM ELAs in each mountain range examined in this study. The dashed lines represent the global boundaries in which temperature and precipitation at modern glacier ELAs has been observed. The blue line was computed from eq. (2) and the black line was computed from eq. (3), known as the climate envelope. The climate envelope describes the T & P needed to sustain glaciers with 65% mass in the accumulation zone.

The Pellitero et al. (2015, 2016) GlaRe and ELA tool present an efficient and accurate reconstruction of paleo-glaciers and ELAs. The GlaRe tool implements a well-established approach for determining the paleo-glaciers equilibrium profile. An approach that alleviates errors that can arise from map-based calculations and reducers the time needed for reconstructing glaciers using traditional map analysis. The GlaRe tool works most efficiently when glacier extents are known from well preserved glacial deposits and landforms, and where flow paths of paleoglaciers followed modern drainage. Without geomorphological limits on past glacier extents and known drainage of the glacial valley, the accuracy of the GlaRe tool is diminished.

Perhaps the greatest advantage of the GlaRe tool is that it allows users to reconstruct paleoglacier across entire mountain ranges using a consistent, physically based set of methods that can be automated in GIS. The Pellitero et al (2015, 2016) tools afford researchers the ability to complete larger-scale glacier and paleoclimate reconstructions in North America and elsewhere. Using Pellitero et al., (2015, 2016) methods, the overall quality of reconstructions improved, while the time needed to produce said reconstructions was greatly reduced.

5. CONCLUSIONS

Climate conditions during the last Pleistocene glaciation in the northeastern Great Basin show a great contrast to modern climate. Globally, during the LGM glaciers reached their maximum extents from 26.5-19.0 ka (Clark et al., 2009). Glaciers in the southwestern region of the United States reached their maxima around the same time. Moreover, the ages of down valley recessional moraine deposition in the southwestern Unites States coincides with ages of down valley recessional moraines found in the Great Basin. TCN exposure age chronologies summarized here across the Great Basin reveal terminal moraines reached their maximum extents from 22-20 ka. placing the regional maxima before the Lake Bonneville high stand (18.0-15.0 ka). Indicating that climate at and before the high stand (19 ka) favored the expansion of glaciers but did not favor the overflow of Lake Bonneville. This suggests that at the end of the LGM, climate in the Bonneville Basin was colder and drier than during the Provo shoreline. Alternatively, if climate had been colder and wetter following the LGM, the Lake Bonneville high stand would have coincided with glacier maxima. The TCN exposure ages show most glaciers reached their down valley recessional moraines during the same time Lake Bonneville was in its overflowing phase (18.0-15.0 ka). This suggests that during the Bonneville high stand, climate favored both the expansion of the lake and presence of glacier advance, supporting a climate that was wetter than the LGM.

Modeling of the climate envelope that encompasses global glacier ELAs and comparing this to modern climate at the LGM ELA in the Great Basin provides an opportunity to infer climate at the LGM. If no change to modern precipitation occurred during the LGM as suggested by Belanger et al. (2021) and Quirk et al. (2020), then ELAs achieved in this study suggest an average regional temperature depression of 10°C. However, given that terminal moraines

reached maximum positions before Lake Bonneville high stand, it is conceivable that precipitation was less than modern at the LGM. If there was a 50% reduction in precipitation at the LGM compared to modern, then a temperature depression of 12°C would have been needed to sustain glaciers at their maxima.

Given that down valley recessional moraines were deposited during the time Lake Bonneville overflowed and that they were close to their maximum length, we can set limits on climate during the 18-15 ka interval based on the ELAs reported here. If, for example, precipitation was double modern during the time Lake Bonneville overflowed, then a temperature depression of 7°C would have been needed to sustain glaciers down valley extents.

The GlaRe tools provide a precise calculation for volume and surface area of paleoglaciers. The volume of ice in the western Uinta icefield (299 km^3) at the LGM constituted for only 4.9% of the total volume of Lake Bonneville (8603 km^3). If, for example, glacier ice would have made up a larger total volume of Lake Bonneville, then it would be plausible to deduce melting glaciers cause the Lake Bonneville overflow. However, since glacier ice makes up such a small percentage of the total volume, glacial melt was not the driving factor in the overflow. This suggests that there was an alternative moisture source that contributed to the Lake Bonneville overflow.

Given the high level of variation found in ELAs in the Ruby Mountains, alone their ELAs are unable provide a reliable estimate of paleoclimate. ELAs in the Ruby Mountains vary 700 m in elevation over a 50 km distance. This amount of variability in the Ruby Mountains shows that paleoclimate interpretations based off singular ranges or valleys alone (Quirk et al., 2020; Belanger et al 2021) are not rigorous enough to provide actual estimates of paleoclimate. To preform accurate regional assessments of paleoclimate using ELAs, a larger quantity of ranges

are needed to reconstruct and analyze climate at the ELA. The GlaRe tools allow for a greater number of ELAs to be calculated quickly and therefore, provides a significant advantage in the precision of paleoclimate reconstructions.

REFERENCES

Balco, G., 2011, Contributions and unrealized potential contributions of cosmogenic-nuclide exposure dating to Glacier Chronology, 1990–2010: Quaternary Science Reviews, v. 30, p. 3–27, doi: 10.1016/j.quascirev.2010.11.003.

Balco, G., 2020, Glacier change and paleoclimate applications of cosmogenic-nuclide exposure dating: Annual Review of Earth and Planetary Sciences, v. 48, p. 21–48, doi: 10.1146/annurev-earth-081619-052609.

Balco, G., 2020, Technical note: A prototype transparent-middle-layer data management and analysis infrastructure for cosmogenic-nuclide exposure dating: Annual Review of Earth and Planetary Sciences, v. 478, doi: 10.5194/gchron-2020-6.

Biek, R., Willis, G., Ehler, B., 2010. Utah's Glacial Geology. Utah Geol. Surv. Notes, 42(3), 1–4.

Belanger, B.K., Amidon, W.H., Laabs, B.J., Munroe, J.S., and Quirk, B.J., 2021, Modelling climate constraints on the formation of Pluvial Lake Bonneville in the Great Basin, United States: Journal of Quaternary Science, doi: 10.1002/jqs.3394.

Benn, D.I., and Hulton, N.R.J., 2010, An EXCELTM spreadsheet program for reconstructing the surface profile of former mountain glaciers and ice caps: Computers & Geosciences, v. 36, p. 605–610, doi: 10.1016/j.cageo.2009.09.016.

Bennett, M.R., and Glasser, N.F., 2013, Glacial Geology: Ice Sheets and landforms: Chichester, Wiley-Blackwell.

Benson, L., Madole, R., Landis, G., and Gosse, J., 2005, New data for late pleistocene pinedale alpine glaciation from southwestern Colorado: Quaternary Science Reviews, v. 24, p. 49–65, doi: 10.1016/j.quascirev.2004.07.018.

Blackwelder, E., 1931, Pleistocene glaciation in the sierra Nevada and Basin Ranges: Geological Society of America Bulletin, v. 42, p. 865–922, doi: 10.1130/gsab-42-865.

Borchers, B., Marrero, S., Balco, G., Caffee, M., Goehring, B., Lifton, N., Nishiizumi, K., Phillips, F., Schaefer, J., and Stone, J., 2016, Geological calibration of spallation production rates in the cronus-earth project: Quaternary Geochronology, v. 31, p. 188–198, doi: 10.1016/j.quageo.2015.01.009.

Clark, P.U., Dyke, A.S., Shakun, J.D., Carlson, A.E., Clark, J., Wohlfarth, B., Mitrovica, J.X., Hostetler, S.W., and McCabe, A.M., 2009, The last glacial maximum: Science, v. 325, p. 710–714, doi: 10.1126/science.1172873.

Denton, G.H., Anderson, R.F., Toggweiler, J.R., Edwards, R.L., Schaefer, J.M., and Putnam, A.E., 2010, The Last Glacial Termination: Science, v. 328, p. 1652–1656, doi: 10.1126/science.1184119.

Ehlers Jürgen, and Gibbard, P.L., 2005, Quaternary glaciations. extent and chronology: Elsevier.

Furbish, D.J., and Andrews, J.T., 1984, The use of hypsometry to indicate long-term stability and response of valley glaciers to changes in mass transfer: Journal of Glaciology, v. 30, p. 199–211, doi: 10.3189/s0022143000005931.

Gradstein, F.M., Ogg, J.G., and Hilgen, F.J., 2012, On the Geologic Time Scale: Newsletters on Stratigraphy, v. 45, p. 171–188, doi: 10.1127/0078-0421/2012/0020.

Hague, A., Emmons, S.F., Humphreys, A.A., and King, C., 1877, Descriptive Geology: Washington, DC, Gov. Print. Off, v. 2.

Hambrey, M., and Alean Jürg, 2004, Glaciers: Cambridge, Cambridge University Press.

Hostetler, S.W., Giorgi, F., Bates, G.T., and Bartlein, P.J., 1994, Lake-atmosphere feedbacks associated with Paleolakes Bonneville and Lahontan: Science, v. 263, p. 665–668, doi: 10.1126/science.263.5147.665.

Laabs, B.J., Marchetti, D.W., Munroe, J.S., Refsnider, K.A., Gosse, J.C., Lips, E.W., Becker, R.A., Mickelson, D.M., and Singer, B.S., 2011, Chronology of latest pleistocene mountain glaciation in the western Wasatch Mountains, Utah, U.S.A.: Quaternary Research, v. 76, p. 272–284, doi: 10.1016/j.yqres.2011.06.016.

Laabs, B.J.C., and Munroe, J.S., 2016, Late pleistocene mountain glaciation in the Lake Bonneville Basin: Lake Bonneville - A Scientific Update, p. 462–503, doi: 10.1016/b978-0-444-63590-7.00017-2.

Laabs, B.J.C., and Munroe, J.S., 2016, Late pleistocene mountain glaciation in the Lake Bonneville Basin: Lake Bonneville - A Scientific Update, v. 20, p. 462–503, doi: 10.1016/b978-0-444-63590-7.00017-2.

Laabs, B.J.C., Licciardi, J.M., Leonard, E.M., Munroe, J.S., and Marchetti, D.W., 2020, Updated cosmogenic chronologies of Pleistocene Mountain Glaciation in the western United States and associated paleoclimate inferences: Quaternary Science Reviews, v. 242, p. 106427, doi: 10.1016/j.quascirev.2020.106427.

Laabs, B.J.C., Munroe, J.S., Best, L.C., and Caffee, M.W., 2013, Timing of the last glaciation and subsequent deglaciation in the Ruby Mountains, Great Basin, USA: Earth and Planetary Science Letters, v. 361, p. 16–25, doi: 10.1016/j.epsl.2012.11.018.

Lake Bonneville, 1890, Washington, United States Geological Survey, v. 1.

Lal, D., and Peters, B., 1967, Cosmic Ray produced radioactivity on the Earth: Kosmische Strahlung II / Cosmic Rays II, p. 551–612, doi: 10.1007/978-3-642-46079-1_7.

Lal, D., and Peters, B., 1967, Cosmic Ray produced radioactivity on the Earth: Kosmische Strahlung II / Cosmic Rays II, p. 551–612, doi: 10.1007/978-3-642-46079-1_7.

Leonard, E., 2007, Modeled patterns of late pleistocene glacier inception and growth in the southern and central Rocky Mountains, USA: Sensitivity to climate change and paleoclimatic implications: Quaternary Science Reviews, v. 26, p. 2152–2166, doi: 10.1016/j.quascirev.2007.02.013.

Leonard, E.M., 1989, Climatic change in the Colorado Rocky Mountains: Estimates based on modern climate at late pleistocene equilibrium lines: Arctic and Alpine Research, v. 21, p. 245, doi: 10.2307/1551563.

Licciardi, J.M., Clark, P.U., Brook, E.J., Elmore, D., and Sharma, P., 2004, Variable responses of Western U.S. glaciers during the last deglaciation: Geology, v. 32, p. 81, doi: 10.1130/g19868.1.

Lifton, N., Sato, T., and Dunai, T.J., 2014, Scaling in situ cosmogenic nuclide production rates using analytical approximations to atmospheric cosmic-ray fluxes: Earth and Planetary Science Letters, v. 386, p. 149–160, doi: 10.1016/j.epsl.2013.10.052.

Lisiecki, L.E., and Raymo, M.E., 2005, A Pliocene-Pleistocene stack of 57 Globally Distributed Benthic Δ18O Records: Paleoceanography, v. 20, doi: 10.1029/2004pa001071.

Loewe, F., 1971, Considerations on the origin of the quaternary ice sheet of North America: Arctic and Alpine Research, v. 3, p. 331–344, doi: 10.1080/00040851.1971.12003623.

Marchetti, D.W., Cerling, T.E., and Lips, E.W., 2005, A glacial chronology for the Fish Creek drainage of Boulder Mountain, Utah, USA: Quaternary Research, v. 64, p. 264–271, doi: 10.1016/j.yqres.2005.05.004.

Marchetti, D.W., Cerling, T.E., Dohrenwend, J.C., and Gallin, W., 2007, Ages and significance of glacial and mass movement deposits on the west side of Boulder Mountain, Utah, USA: Palaeogeography, Palaeoclimatology, Palaeoecology, v. 252, p. 503–513, doi: 10.1016/j.palaeo.2007.05.016.

Meierding, T.C., 1982, Late pleistocene glacial equilibrium-line altitudes in the Colorado Front Range: A comparison of methods: Quaternary Research, v. 18, p. 289–310, doi: 10.1016/0033-5894(82)90076-x.

Moore, E.M.M., Eaves, S.R., Norton, K.P., Mackintosh, A.N., Anderson, B.M., Dowling, L.H., and Hidy, A.J., 2022, Climate reconstructions for the last glacial maximum from a simple Cirque Glacier in Fiordland, New Zealand: Quaternary Science Reviews, v. 275, p. 107281, doi: 10.1016/j.quascirev.2021.107281.

Munroe, J.S., and Mickelson, D.M., 2002, Last Glacial Maximum equilibrium-line altitudes and paleoclimate, Northern Uinta Mountains, Utah, U.S.A.: Journal of Glaciology, v. 48, p. 257–266, doi: 10.3189/172756502781831331.

Munroe, J.S., Laabs, B.J.C., Shakun, J.D., Singer, B.S., Mickelson, D.M., Refsnider, K.A., and Caffee, M.W., 2006, Latest pleistocene advance of alpine glaciers in the southwestern Uinta Mountains, Utah, USA: Evidence for the influence of local moisture sources: Geology, v. 34, p. 841, doi: 10.1130/g22681.1.

O'Connor, J.E., and Costa, J.E., 1993, Geologic and hydrologic hazards in glacierized basins in North America resulting from 19th and 20th century global warming: Natural Hazards, v. 8, p. 121–140, doi: 10.1007/bf00605437.

Ohmura, A., Kasser, P., and Funk, M., 1992, Climate at the equilibrium line of glaciers: Journal of Glaciology, v. 38, p. 397–411, doi: 10.3189/s0022143000002276.

Osborn, G., 2001, Glaciation in the Great Basin of the Western United States: Quaternary Science Reviews, v. 20, p. 1377–1410, doi: 10.1016/s0277-3791(01)00002-6.

Oster, J.L., Ibarra, D.E., Winnick, M.J., and Maher, K., 2015, Steering of westerly storms over western North America at the Last Glacial Maximum: Nature Geoscience, v. 8, p. 201–205, doi: 10.1038/ngeo2365.

Oviatt, C.G., 2015, Chronology of lake bonneville, 30,000 to 10,000 yr B.P.: Quaternary Science Reviews, v. 110, p. 166–171, doi: 10.1016/j.quascirev.2014.12.016.

Pellitero, R., Rea, B.R., Spagnolo, M., Bakke, J., Hughes, P., Ivy-Ochs, S., Lukas, S., and Ribolini, A., 2015, A GIS tool for automatic calculation of Glacier equilibrium-line altitudes: Computers & Geosciences, v. 82, p. 55–62, doi: 10.1016/j.cageo.2015.05.005.

Pellitero, R., Rea, B.R., Spagnolo, M., Bakke, J., Ivy-Ochs, S., Frew, C.R., Hughes, P., Ribolini, A., Lukas, S., and Renssen, H., 2016, Glare, a GIS tool to reconstruct the 3D surface of palaeoglaciers: Computers & Geosciences, v. 94, p. 77–85, doi: 10.1016/j.cageo.2016.06.008.

Porter, S.C., and Swanson, T.W., 2008, 36Cl dating of the classic pleistocene glacial record in the northeastern Cascade Range, Washington: American Journal of Science, v. 308, p. 813–813, doi: 10.2475/06.2008.04.

Quirk, B.J., Moore, J.R., Laabs, B.J.C., Plummer, M.A., and Caffee, M.W., 2020, Latest pleistocene glacial and climate history of the Wasatch Range, Utah: Quaternary Science Reviews, v. 238, p. 106313, doi: 10.1016/j.quascirev.2020.106313.

Rea, B.R., 2009, Defining modern day area-altitude balance ratios (aabrs) and their use in glacier-climate reconstructions: Quaternary Science Reviews, v. 28, p. 237–248, doi: 10.1016/j.quascirev.2008.10.011.

Shakun, J.D., Clark, P.U., He, F., Lifton, N.A., Liu, Z., and Otto-Bliesner, B.L., 2015, Regional and global forcing of Glacier Retreat during the last deglaciation: Nature Communications, v. 6, doi: 10.1038/ncomms9059.

Thompson, L.G., Davis, M.E., Mosley-Thompson, E., Porter, S.E., Corrales, G.V., Shuman, C.A., and Tucker, C.J., 2021, The impacts of warming on rapidly retreating high-altitude, low-latitude glaciers and Ice Core-derived climate records: Global and Planetary Change, v. 203, p. 103538, doi: 10.1016/j.gloplacha.2021.103538.

Wayne, W.J., 1984, Glacial Chronology of the ruby mountains-east humboldt range, Nevada: Quaternary Research, v. 21, p. 286–303, doi: 10.1016/0033-5894(84)90069-3.

Wesnousky, S.G., Briggs, R.W., Caffee, M.W., Ryerson, F.J., Finkel, R.C., and Owen, L.A., 2016, Terrestrial cosmogenic surface exposure dating of glacial and associated landforms in the Ruby Mountains-East humboldt range of central Nevada and along the northeastern flank of the Sierra Nevada: Geomorphology, v. 268, p. 72–81, doi: 10.1016/j.geomorph.2016.04.027.

Young, N.E., Briner, J.P., Leonard, E.M., Licciardi, J.M., and Lee, K., 2011, Assessing climatic and nonclimatic forcing of Pinedale glaciation and deglaciation in the Western United States: Geology, v. 39, p. 171–174, doi: 10.1130/g31527.1.

Zielinski, G.A., and McCoy, W.D., 1987, Paleoclimatic implications of the relationship between modern snowpack and late pleistocene equilibrium-line altitudes in the mountains of the Great Basin, Western U.S.A.: Arctic and Alpine Research, v. 19, p. 127, doi: 10.2307/1551246.

APPENDIX A. MODEL BUILDER OF GLARE AND ELA TOOLS

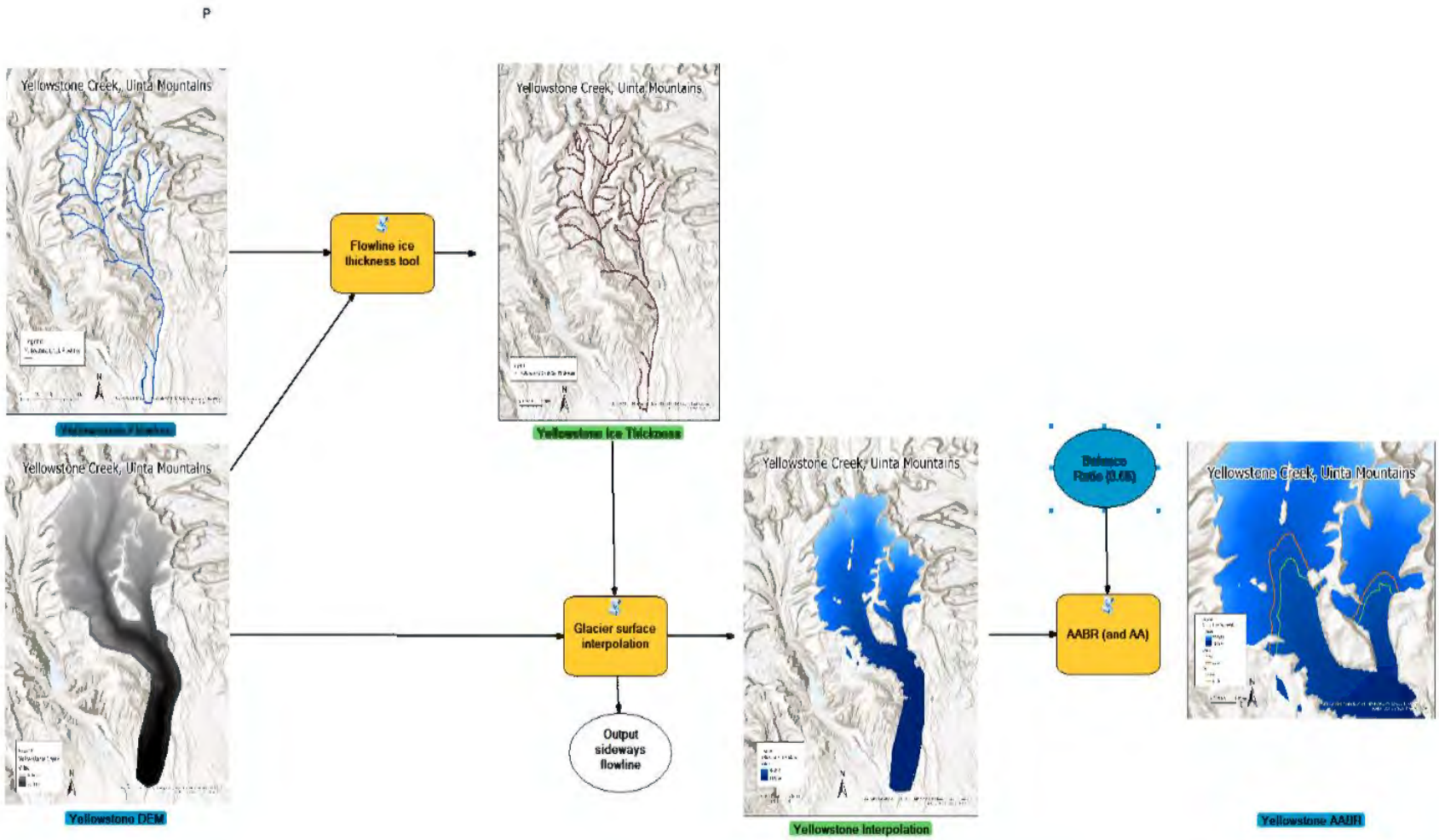
P
Yellowstone Creek, Uinta Mountains
Flowline ice thickness tool
Yellowstone Creek, Uinta Mountains
Yellowstone Ice Thickness
Yellowstone Creek, Uinta Mountains
Yellowstone DEM
Glacier surface interpolation
Output sideways flowline
Yellowstone Creek, Uinta Mountains
Yellowstone Interpolation
Balance Ratio (0.68)
AABR (and AA)
Yellowstone Creek, Uinta Mountains
Yellowstone AABR

A.1 Model Builder for Glare and ELA Tools

```
# Import arcpy module
import arcpy
# Load required toolboxes

arcpy.
ImportToolbox("C:/Users/benja/OneDrive/Desktop/ELAs_InBB/Tools_E
LA_GLARE (1)/Pellitero-2015-master/ELA_calculation_toolbox.tbx")
# Script arguments
Yellowstone_Flowline = arcpy.GetParameterAsText(0)
if Yellowstone_Flowline == '#' or not Yellowstone_Flowline:
    Yellowstone_Flowline =
"C:\\Users\\benja\\OneDrive\\Desktop\\ELAs_InBB\\Uinta\\Yellowst
one Creek\\Flowlines\\YellowSFlow.shp" # provide a default value
if unspecified

Yellowstone_DEM = arcpy.GetParameterAsText(1)
if Yellowstone_DEM == '#' or not Yellowstone_DEM:
    Yellowstone_DEM =
"C:\\Users\\benja\\OneDrive\\Desktop\\ELAs_InBB\\Uinta\\Yellowst
one Creek\\Watershed\\yellowsdem" # provide a default value if
unspecified

# Local variables:
Yellowstone_Ice_Thickness =
"C:\\Users\\benja\\OneDrive\\Desktop\\ELAs_InBB\\Uinta\\Yellowst
one Creek\\Ice Thickness\\Yellow.shp"
Output_sideways_flowline_propagation = ""
Yellowstone_Interpolation =
"C:\\Users\\benja\\OneDrive\\Desktop\\ELAs_InBB\\Uinta\\Yellowst
one Creek\\Interpolation\\yeelwo"
Balance_Ratio__0_65_ =
"C:\\Users\\benja\\OneDrive\\Desktop\\ELAs_InBB\\Uinta\\Yellowst
one Creek\\AABR_AA"

# Process: Flowline ice thickness tool
arcpy.gp.toolbox = "c:/program files
(x86)/arcgis/desktop10.3/ArcToolbox/Toolboxes/GLARE.tbx";
# Warning: the toolbox c:/program files
(x86)/arcgis/desktop10.3/ArcToolbox/Toolboxes/GLARE.tbx DOES NOT
have an alias.
# Please assign this toolbox an alias to avoid tool name
collisions
# And replace arcpy.gp.Flowlineicethickness2(...) with
arcpy.Flowlineicethickness2_ALIAS(...)
```

```
arcpy.gp.Flowlineicethickness2(Yellowstone_DEM,
Yellowstone_Flowline, "50", Yellowstone_Ice_Thickness, "100000")

# Process: Glacier surface interpolation
arcpy.gp.toolbox = "c:/program files
(x86)/arcgis/desktop10.3/ArcToolbox/Toolboxes/GLARE.tbx";
# Warning: the toolbox c:/program files
(x86)/arcgis/desktop10.3/ArcToolbox/Toolboxes/GLARE.tbx DOES NOT
have an alias.
# Please assign this toolbox an alias to avoid tool name
collisions
# And replace arcpy.gp.Surface(...) with
arcpy.Surface_ALIAS(...)
arcpy.gp.Surface(Yellowstone_Ice_Thickness, Yellowstone_DEM, "",
"200", "TOPO TO RASTER", Output_sideways_flowline_propagation,
Yellowstone_Interpolation)

# Process: AABR (and AA)
arcpy.gp.toolbox =
"C:/Users/benja/OneDrive/Desktop/ELAs_InBB/Tools_ELA_GLARE
(1)/Pellitero-2015-master/ELA_calculation_toolbox.tbx";
# Warning: the toolbox
C:/Users/benja/OneDrive/Desktop/ELAs_InBB/Tools_ELA_GLARE
(1)/Pellitero-2015-master/ELA_calculation_toolbox.tbx DOES NOT
have an alias.
# Please assign this toolbox an alias to avoid tool name
collisions
# And replace arcpy.gp.AABR(...) with arcpy.AABR_ALIAS(...)
arcpy.gp.AABR(Yellowstone_Interpolation, Balance_Ratio__0_65_,
"50", "0.65")
```

APPENDIX B. SUPPLEMENTAL TABLES

Table B1. Deep Creek Range ELA (n=6)

Valley	AABR (m asl)
Granite Creek	3168
Haystack Creek	3215
Red Creek	3220
Steves Creek south	2889
Steves Creek north	2862
Big Hole	2665

Table B2. East Humboldt Range ELAs (n=24)

Valley	AABR (m asl)
Ackler Left Creek	2765
Ackler Right Creek	2727
Boulder Creek First	2755
Boulder Creek Fourth	2678
Boulder Creek Third	2796
Clover Creek	2632
Franklin Creek	2771
Greyes Creek	2578
Herder Creek Middle Fork	2606
Herder Creek North Fork	2589
Herder Creek South Fork	2588
Johnson Creek	2577
Leach Creek	2751
North Fork Angel Creek	2670
Pole Canyon	2771
Schoer Creek	2753
South Fork Angel Creek	2808
South Fork Steele Creek	2767
Steele Creek	2815
Trout Creek	2579
Weeks Creek	2688
Willow Creek	2670
Winchell Creek	2674
Wiseman Creek	2685

Table B3. Independence Mountains ELAs (n=13)

Valley	AABR (m asl)
Beadles Creek	2540
Chicken Creek	2532
Dry Creek	2597
Foreman Creek	2556
McAfee Creek	2726
Mill Creek	2640
North Fork Pratt Creek	2600
Peterson Creek	2633
Pratt Creek	2639
Pratt Tribe Creek	2745
Rim Creek	2532
Sammy Creek	2477
Walker Creek	2637

Table B4. Oquirrh Range ELAs (n=4)

Valley	AABR (m asl)
Big Hole	2665
Jackson Hollow	2763
Lowe Canyon	2741
Settlement Canyon	2844

Table B5. Ruby Mountains ELAs (n=92)

Valley	AABR (m asl)
Battle North	2913
Battle South	2798
Brennen	2562
Campbell Right	2841
Campbell Left	2782
Carter Creek	2788
Colonel Moore Creek Middle	2890
Colonel Moore Creek North	2864
Colonel Moore Creek South	2775
Conrad Creek	2717
Dads Creek Four	2614
Dads Creek One	2807
Dads Creek Three	2843
Dads Creek Two	2755
Dawleys Creek	2778
Echo Creek	2920
Franklin Creek	2635
Furlong Creek	2894
Gendey Creek	2794
Gennette Creek	2681
Green Mountain	2829
Griswold North Creek	2925
Griswold South Creek	2916
Hankins Creek	2884
John Day Creek Left	2732
John Day Creek Middle	2878
John Day Creek Right	2923
Kleckner Creek	2875
Krenka Creek	2682
Lamoille 1	2780
Lamoille 2	2920
Lamoille 3	2853
Lamoille 4	2838
Lamoille 5	2948
Lamoille Main	2858
Little Cottonwood Creek	2353
Long Creek	2748
Lutts Creek 2	2830
Lutts Creek 4	3014
Lutts Creek 5	3060
Lutts Creek 6	2786
Mahogany Creek	2842
Mayhew Middle Creek	2769
Mayhew North Creek	2951
Mayhew South Creek	2814
McCutcheon North	2951
McCutcheon South	2831
Middle Fork Cold Creek	2762
Murphy Creek	2538
Myers North Creek	2821
Myers South Creek	2921
North Fork Cold Creek	2832

Table B5. Ruby Mountains ELAs (continued).

Valley	AABR (m asl)
North Fork Smith Creek	2824
Overland Creek 1	2893
Overland Creek 2	2730
Overland Creek 3	2846
Overland Creek 5	2811
Overland Creek 6	2786
Rabbit Creek	2762
Rattle Snake Creek Left	2859
Rattle Snake Creek Middle	2739
Rattle Snake Creek Right	2798
Right Fork Left Lamoille	2682
Right Fork Middle Lamoille	2913
Right Fork Right Lamoille	2822
Robinson Creek	2884
Ross Creek	2730
Secrets Peak East	2483
Secrets Peak West	2433
Segunda Creek	2762
Seitz Canyon	2760
Sharps Creek North	2682
Sharps Creek South	2720
Soldier Creek 2	2573
Soldier Creek 3	2678
Soldier Creek 4	2802
Soldier Creek 6	2784
South Fork Cold Creek	2806
Starvation Canyon	2521
Stoddard Creek	2843
Talbot Creek Left	2757
Talbot Creek Right	2893
Thompson Creek North	2820
Thompson Creek South	2752
Thorpe Creek North	2932
Thorpe Creek South	2842
Tipton Creek	2867
Wilson Creek North	2736
Wilson Creek South	2711
Wines Creek	2759
Withington	2812
Young Creek	2740

Table B6. South Snake Range ELAs (n=10)

Valley	AABR (m asl)
Blue Canyon Left	3091
Blue Canyon Middle	2992
Blue Canyon Right	2981
Lehman Creek	3128
North Fork Baker Creek	3114
Snake Creek Middle	3108
Snake Creek North	3106
Snake Creek South	3115
South Fork Baker Creek	3073
Williams Creek	2962

Table B7. Stansbury Range ELAs (n=8)

Valley	AABR (m asl)
Big Creek Canyon	2745
Big Pole Canyon	2714
Little Pole Canyon	2771
Mining Fork Creek	2607
North Willow Canyon	2618
Pass Canyon	2649
South Willow Canyon	2679
Spring Canyon	2916

Table B8. Uinta Mountains ELAs (n= 46)

Valley	AABR (m asl)
Bear Basin	2636
Black Fort	3458
Blind Stream	3079
Broad Canyon	2918
Burnt Fork	3397
Burnt Ridge	3092
Chalk Creek	2953
Crow Canyon	3308
Deer Creek	3052
Dry Fork Creek	3324
Duchesne Creek	3111
East Fork Carter Creek	3211
East Fork Smith Creek	3459
East Fork Bear Creek	3203
Hayden Fork Bear River	3203
Heller Lake	3181
Henerys Fork	3399
Krebs Basin	3346
Lake Fork	3285
Middle Fork Beaver Creek	3316
Middle Fork Sheep Creek	3303
Mill Fork	2813
Noblettes Creek	2571
North Fork Provo	3026
North Fork Ashley Creek	3324
Pole Creek	3345
Rock Creek	3237
Shingle Mill East	2799
Slader Creek	2904
Smith and Morehouse	2966
South Fork Ashley Creek	3330
South Fork Sheep Creek	3295
Split Creek	3254
Swift Canyon	2775
Thompson Creek	3269
Weber River	3057
West Fork Bear River	2881
West Fork Beaver River	3284
West Fork Carter River	3273
West Fork Smith Fork	3310
White Pine Canyon	2777
Whiterocks	3381
Wolfe Creek	2891
Yellow Pine Creek	2905
Yellowstone Creek	3303
South Fork Weber Creek	2830

Table B9. Wasatch Range ELAs (n=50)

Valley	AABR (m asl)
Alexander Basin	2713
American Fork Snake Creek	2794
Bartholomew Canyon	2606
Bells Canyon	2825
Big Cottonwood Canyon	2805
Big Spring Hollow	2398
Big Willow Creek	2776
Box Elder Canyon	2899
Bunnells Fork	2390
Burnt Hollow	2718
Butter Fork	2779
Chipman Canyon	2880
Corral Mountain	2796
Deer Creek	2528
Dry Creek	2758
Dry Fork	2734
Dutch Draw	2654
First Hole	2765
Fourth Hole	2700
Little Cottonwood Canyon	2751
Little Willow Canyon	2876
Major Evans Gulch	2766
Middle Fork Dry Creek	2582
Mill A Basin	2786
Mill B North Fork	2701
Mill D North Fork	2848
Newton Canyon	2830
North Bartholomew Canyon	2715
North Fork Deaf Smith Canyon	2772
Pole Canyon 1	2620
Pole Canyon 2	2636
Prime Rose Cirque	2501
Red Pine Canyon	2722
Rock Canyon	2505
Rocky Mouth Canyon	2652
S Bartholomew Canyon	2707
Second Hole	2731
Shingle Mill Canyon	2505
Silver Fork	2815
Snake Creek	2637
Snowslide Canyon	2852
South Fork Dry Creek	2657
South Fork Dry Creek	2063
Thaynes Canyon	2592
Third Hole	2684
Tibble Fork	2404
Walker and Webster Gulch	2753
White Pine Canyon	2821
Whittemore Canyon	2622
Wilson Fork	2715